Article

Current Biology

Live Observation of Two Parallel Membrane Degradation Pathways at Axon Terminals

Highlights

- Membrane protein degradation can occur at axon terminals
- Two parallel mechanisms degrade synaptic vesicle and plasma membrane proteins
- The two mechanisms are molecularly distinct and employ different cathepsins
- Local "hub" compartments bud off retrograde vesicles at any maturation stage

Authors

Eugene Jennifer Jin, Ferdi Ridvan Kiral, Mehmet Neset Ozel, ..., Heike Wolfenberg, Steffen Prohaska, Peter Robin Hiesinger

Correspondence

robin.hiesinger@fu-berlin.de

In Brief

Jin et al. develop a live-imaging method based on acidification-sensing probes in intact *Drosophila* brains to reveal two molecularly distinct endolysosomal degradation pathways at axon terminals. Independent of the canonical Rab7-dependent pathway, synaptic vesicle protein degradation requires n-Syb, V100, and Cathepsin L-like protease Cp1.

Jin et al., 2018, Current Biology *28*, 1027–1038
April 2, 2018
https://doi.org/10.1016/j.cub.2018.02.032

CellPress

Current Biology
Article

Live Observation of Two Parallel Membrane Degradation Pathways at Axon Terminals

Eugene Jennifer Jin,[1,2,5] Ferdi Ridvan Kiral,[1,5] Mehmet Neset Ozel,[1,2] Lara Sophie Burchardt,[1] Marc Osterland,[3] Daniel Epstein,[1,4] Heike Wolfenberg,[1] Steffen Prohaska,[3] and Peter Robin Hiesinger[1,6,*]
[1]Division of Neurobiology, Freie Universität Berlin, Königin Luise Straße 1-3, 14195 Berlin, Germany
[2]Graduate School of Biomedical Sciences, UT Southwestern Medical Center, Dallas, TX 75390, USA
[3]Zuse Institute Berlin, Takustraße 7, 14195 Berlin, Germany
[4]Present address: Department of Surgery, University of Alabama, Birmingham, Birmingham, AL 35233, USA
[5]These authors contributed equally
[6]Lead Contact
*Correspondence: robin.hiesinger@fu-berlin.de
https://doi.org/10.1016/j.cub.2018.02.032

SUMMARY

Neurons are highly polarized cells that require continuous turnover of membrane proteins at axon terminals to develop, function, and survive. Yet, it is still unclear whether membrane protein degradation requires transport back to the cell body or whether degradation also occurs locally at the axon terminal, where live observation of sorting and degradation has remained a challenge. Here, we report direct observation of two cargo-specific membrane protein degradation mechanisms at axon terminals based on a live-imaging approach in intact *Drosophila* brains. We show that different acidification-sensing cargo probes are sorted into distinct classes of degradative "hub" compartments for synaptic vesicle proteins and plasma membrane proteins at axon terminals. Sorting and degradation of the two cargoes in the separate hubs are molecularly distinct. Local sorting of synaptic vesicle proteins for degradation at the axon terminal is, surprisingly, Rab7 independent, whereas sorting of plasma membrane proteins is Rab7 dependent. The cathepsin-like protease CP1 is specific to synaptic vesicle hubs, and its delivery requires the vesicle SNARE neuronal synaptobrevin. Cargo separation only occurs at the axon terminal, whereas degradative compartments at the cell body are mixed. These data show that at least two local, molecularly distinct pathways sort membrane cargo for degradation specifically at the axon terminal, whereas degradation can occur both at the terminal and *en route* to the cell body.

INTRODUCTION

Neurons must regulate the turnover of membrane proteins in axons, dendrites, and the cell body to ensure normal development and function. Defects in membrane protein degradation are hallmarks of neurodegenerative diseases [1–6]. Recent progress has identified several mechanisms that are required at axon terminals to prevent dysfunction and degeneration, including the local generation of autophagosomes and endolysosomes [7–12]. However, it is unclear whether these degradative organelles are principally transported back to the cell body for degradation or whether degradation can occur locally [9, 13–16]. In addition, the cargo specificity of membrane degradation mechanisms at the axon terminals has remained largely unknown, i.e., it is unclear which membrane proteins are degraded by what mechanisms [16].

Several mechanisms have been directly linked to synapse function or degeneration and have raised questions about cargo specificity and the ultimate locale for degradation. These include (1) local generation of autophagosomes at axon terminals [7, 8], (2) maturation of autophagosomes and endosomes that depends on the ubiquitous small guanosine triphosphatase (GTPase) Rab7 [17, 18], (3) endosomal sorting that depends on the GTPase Rab35 and RabGAP Skywalker [11, 12, 19], and (4) endosomal sorting that depends on the neuron-specific synaptic vesicle (SV) proteins neuronal synaptobrevin (n-Syb) and V100 [20–22]. These mechanisms may overlap, and defects in any of them cause neurodegeneration in a variety of neurons [11, 17, 20, 22–25]. In the case of (macro-) autophagy, the formation of autophagosomes occurs at axon terminals [10, 26, 27], whereas degradation is thought to occur during and after retrograde transport back to the cell body [8, 9, 27]. As with both the canonical and neuron-specific endolysosomal mechanisms, it remains largely unknown what cargoes are sorted into autophagosomes at axon terminals [9, 27]. The Rab35/Skywalker-dependent endosomal sorting mechanism was recently reported to selectively sort different SV proteins in an activity-dependent manner [19]. Lysosomes have also been shown to localize to dendritic spines in an activity-dependent manner [28]. In both cases, it remains unknown whether degradation occurs locally at synapses and what cargo proteins are affected. Finally, we have previously described a "neuronal sort-and-degrade" (NSD) mechanism based on the function of the two neuron-specific synaptic genes *n-syb* and *v100* [20, 22]. Similar to the other mechanisms, neither cargo specificity nor the locale of degradation for NSD is known. For all mechanisms, it has remained a challenge to directly observe their local roles in the context of normal development and function in an intact brain.

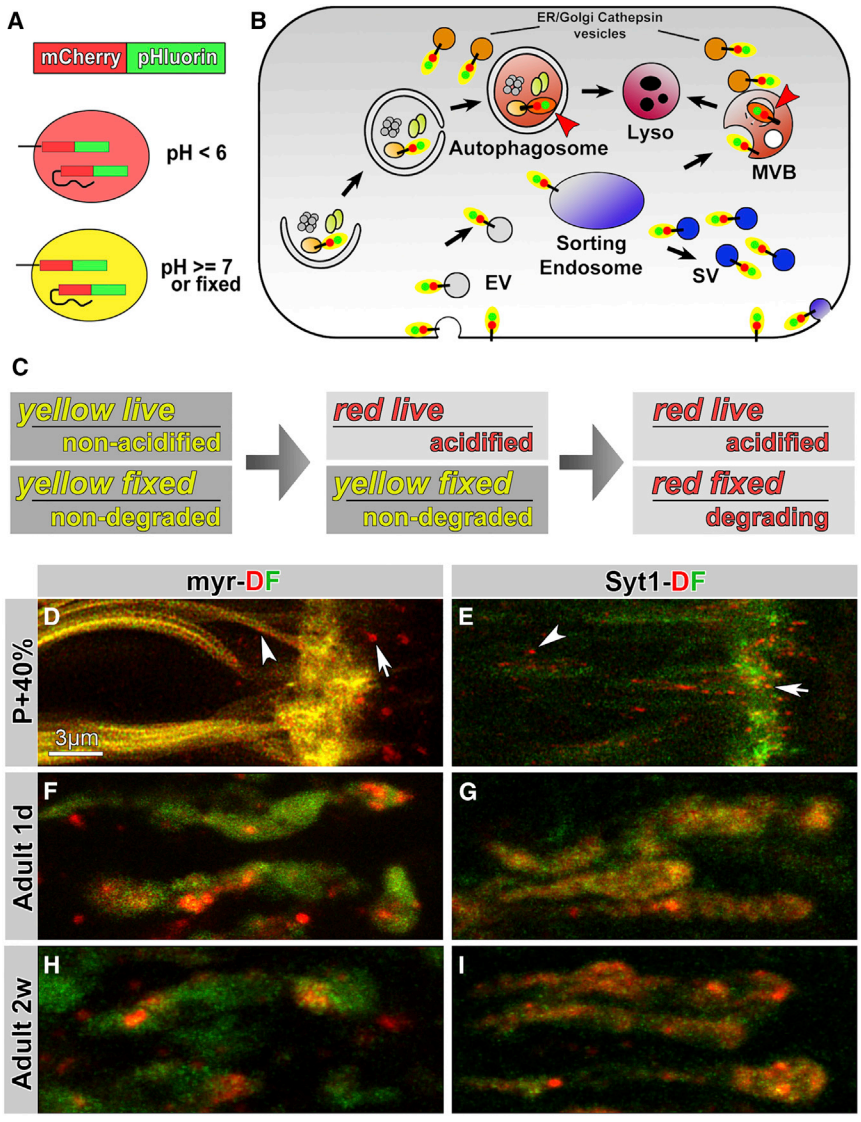

Figure 1. Live Observation of General Plasma Membrane Cargo (myr) and Synaptic-Vesicle-Specific Cargo (Syt1) in Large Acidic Compartments at Axon Terminals

(A) Design of the acidification-sensing dual fluorophore (DF) mCherry-pHluorin tag.

(B) Cytoplasmically DF-tagged proteins "turn red" only in multivesicular bodies (MVBs), lysosomes, and autophagosomes.

(C) The DF tag as acidification and degradation sensor. Acidification sensor: yellow fluorescence live indicates a non-acidic environment; red fluorescence live indicates an acidic environment. Degradation sensor: "yellow fixed" indicates both fluorophores are intact; "red fixed" indicates degradation of the terminal pHluorin tag.

(D–I) Live imaging of myr-DF and Syt1-DF probes in axon terminals of developing (P+40%, 40% pupal development; D and E), 1-day-old (F and G), and 2-week-old adult (H and I) *Drosophila* photoreceptor axon terminals. Arrows, terminal compartments; arrowheads, axonal compartments.

See also Figures S1 and S2 and Movies S1 and S2.

In this study, we report the direct observation of cargo-specific endolysosomal sorting and degradation at axon terminals *in vivo* using live imaging in intact *Drosophila* brains. We define axon terminal "hub" compartments based on their local dynamics, maturation, degradation, continuous mixing through fusion and fission, and budding of retrograde transport vesicles. In addition, we identified two distinct pools of hubs that function locally in two separate endolysosomal pathways based on different cargo specificities, different molecular sorting, and different maturation mechanisms.

RESULTS

We devised a live-imaging approach to directly observe when, where, and with what cargo specificity membrane protein turnover and degradation occur in neurons in an intact brain. Our approach is based on two improved methods that make use of advantages of the *Drosophila* system: first, a recently developed eye-brain culture system for continuous fast live imaging at subcellular resolution in neurons inside an intact brain from early development up to adulthood [29], and second, genetically encoded dual fluorophore live-imaging probes that quantitatively measure when and where they are sorted into degradative compartments.

Live Observation of Large Acidic Compartments at Axon Terminals

Genetically encoded fusions with pHluorin, a pH-sensitive GFP, and mCherry, a particularly pH-resistant red fluorescent protein (RFP), report cargo incorporation into degradative membrane compartments [30, 31] (Figures 1A and 1B). The approach is designed to measure both sorting and degradation: cytosolic fusions of the dual fluorophore (DF) tag to membrane proteins retain yellow fluorescence during normal cycles of exo-/endocytosis, including the entire SV cycle, and shift from yellow to red fluorescence only after engulfment into the strongly acidified environments of multivesicular bodies or autophagosomes (Figure 1B).

In addition, the DF tag can visualize partial degradation if only one of the two fluorophores is degraded (Figure 1C). pHluorin is both more sensitive to fluorescence loss and more exposed to proteases when fused in the terminal position (Figures 1A and 1B). We reasoned that fusion proteins on early endosomal compartments and cytoplasmically exposed membranes should retain yellow fluorescence both live and fixed ("yellow live" in Figure 1C). Engulfment into strongly acidified compartments should initially lead to "red live" fluorescence that can be reverted to yellow when fixed. Finally, initiation of degradation should lead to irreversible damage of pHluorin first and thereby to "red fixed" fluorescence (Figure 1C).

We designed two imaging probes: first, a general membrane cargo by fusing the DF tag to a myristoylated residue with the

idea to mark most membranes in an unbiased manner (myr-DF), and second, a fusion of the DF tag to the highly specific SV membrane protein Synaptotagmin 1 (Syt1-DF) [32]. We performed live imaging of the two probes in developing photoreceptor axon terminals starting prior to synaptogenesis (40% of pupal development [P+40%]) and in 1-day- and 2-week-old adults (Figures 1D–1I). The myr-DF probe exhibited widespread membrane labeling, whereas Syt1-DF was more restricted to the axon terminals. Both probes marked clearly discernible intracellular membrane compartments in axons (arrowheads in Figures 1D and 1E) and at axon terminals (arrows). We expected to see both acidified and non-acidified compartments, but surprisingly, yellow or green fluorescence appeared always diffuse or, in the case of myr-DF, on the plasma membrane. Diffuse yellow labeling of terminals in the case of Syt1-DF most likely represents pools of SVs. In contrast, all distinctly recognizable compartments lacked the pHluorin signal and appeared red live, indicating an acidified environment below pH 6 [20, 30] (Figures 1D–1I; Movie S1). We made similar observations in photoreceptor neuron cell bodies and at axon terminals and in cell bodies of class IV sensory neurons in intact larvae (Figures S1A and S1B). We chose P+40% photoreceptor neuron terminals for the majority of wild-type and mutant imaging analyses, because all mutants used in this study exhibited membrane degradation defects starting at this stage (see below). Secondary effects, including an upregulation of autophagy, subsequently mask the primary endolysosomal functions and defects in sorting and degradation of cargo proteins [13, 22].

The presence of large, acidified compartments suggests that packaging of synaptic membrane cargo into degradative compartments, and possibly degradation itself, can occur locally at axon terminals. Furthermore, we were surprised that Syt1-DF may be subject to turnover and degradation before functional synapses exist. We therefore tested whether our imaging probes are faithful reporters of local degradative compartments in a series of experiments as follows.

First, we tested whether expression of either probe alters endomembrane compartments, degradation, or neuronal function. Immunohistochemical analyses indicate that neither probe alters endogenous levels of endosomes, lysosomes, or autophagosomes in either axon terminals or cell bodies based on several markers in quantitative clonal comparisons (Figures S1C–S1G); in addition, neither probe alters neuronal function based on electroretinogram recordings in adult flies (Figures S1H and S1I). Second, Syt1-DF is expressed at levels comparable to endogenous Syt1 at axon terminals (Figures S2A and S2B); similar to the probe, endogenous Syt1 is made and transported to axon terminals as early as P+10% (Figures S2C–S2F; Movie S2) and both endogenous Syt1 and the Syt1-DF probe are sorted into lysosomal compartments indistinguishably (Figures S2G–S2I). Third, we confirmed with electrophysiology, live imaging, and immunohistochemistry that C-terminally tagged Syt1-DF is sorted and degraded indistinguishably from N-terminally tagged DF-Syt1, despite being a less functional protein [33] (Figures S2J–S2N). Importantly, DF-Syt1 is less useful for our purpose, because it is a sensor for SV acidification, similar to numerous probes facing the vesicular lumen, which are prominently used to measure synaptic function and single SV exocytosis [34]. In contrast, cytoplasmically tagged Syt1-DF selectively turns red live only when sorted into a multivesicular body or autophagosome (Figure 1B). Findings were validated in fixed preparations using both Syt1 probes throughout the study. We conclude that both the myr-DF and Syt1-DF imaging probes faithfully report the local incorporation of synaptic membrane proteins into large, acidic compartments at axon terminals. Furthermore, because Syt1 has no developmental function in photoreceptor neurons [22, 35], its early turnover indicates that photoreceptor neurons activate synaptic maintenance machinery prior to synaptic function.

Degradation Starts at Axon Terminals

Fixation of red-live compartments should cause full reversion of intact DF tags to yellow fluorescence due to the reversibility of pHluorin quenching, whereas degradation of pHluorin should lead to red-fixed compartments (Figure 1C). We found that 14% of myr-DF and 8% of Syt1-DF-positive axon terminal compartments did not regain pHluorin fluorescence through fixation (Figures 2A–2E and 2G). To test whether red-fixed compartments represent late-stage degradative compartments, we performed co-labeling with the lysosomal marker Spinster and the early endosomal marker Rab5. Indeed, red-fixed compartments were 2- to 3-fold more positive for the lysosomal marker, whereas yellow-fixed compartments were 2- to 3-fold more positive for the early endosomal marker (Figures 2F and 2H). These results indicate that some pHluorin is degraded in late-stage lysosomal compartments at axon terminals. We conclude that degradation of both probes is initiated in the axon terminal, and we therefore refer to these late-stage endolysosomal compartments as ''degradative compartments''.

Next, we asked whether trafficking vesicles in the axon are selectively late-stage degradative compartments. Surprisingly, co-labeling of axonal trafficking vesicles with Rab5 and Spin revealed a mixture very similar to axon terminal compartments (Figures 2I–2L). These findings suggest that axonal vesicles for retrograde trafficking are not selected for their degradative state but instead can enter retrograde trafficking at any stage of maturation.

To investigate the nature of degradative compartments, we tested, in addition to Rab5 and Spin, the late endosomal marker Rab7, the recycling endosomal marker Rab11, the synaptic endosomal marker Skywalker, and the autophagosome marker Atg8 [12, 20, 36, 37]. All six markers colocalized 8%–25% with both Syt1- and myr-DF-positive compartments (Figures 2M and S3). Note that low levels of colocalization are expected for dynamically changing markers as compartments mature, e.g., conversion from Rab5 to Rab7 [38, 39]. Importantly, red-fixed compartments predominantly colocalize with degradative compartment markers Rab7 and Atg8, in addition to Spin, but not with the endosomal markers Rab5, Rab11, and Sky, corroborating the local initiation of degradation in late-stage compartments (red bars in Figure 2M). Finally, only late-stage compartments, marked by Rab7 and Atg8, exhibited significantly increased labeling of myr-DF compared to Syt1-DF, suggesting a possible difference between the two probes (Figure 2M).

Local Hub Compartments Are in Continuous Flux and Bud off Retrograde Trafficking Vesicles

To understand their different local dynamics, stability, and retrograde trafficking, we tracked Syt1-DF and myr-DF acidic

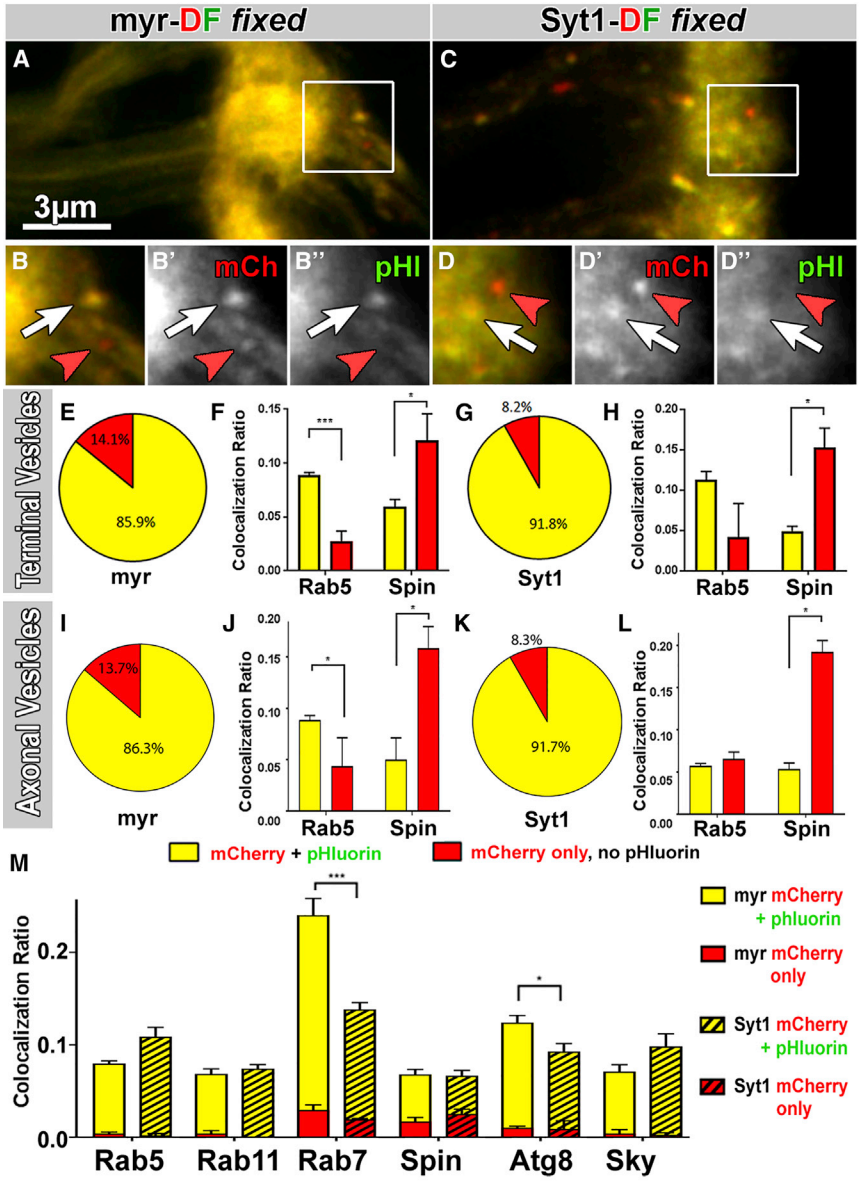

Figure 2. Degradation Starts at Axon Terminals

(A–D″) Some terminal compartments remain "red only" after fixation (red arrowheads), indicating irreversible damage of pHluorin for both myr-DF (A–B″) and Syt1-DF (C–D″). White arrows mark yellow-fixed compartments.

(E–L) Red-only compartments after fixation are late-stage degradative compartments. Pie charts show ratios of mCherry-only versus yellow terminal compartments (E and G) and axonal vesicles (I and K). Bar charts in (F), (H), (J), and (L) show colocalization ratios of yellow-fixed and red-fixed compartments separately with the early endosomal marker Rab5 and the lysosomal marker Spin (F, H, J, and L). Mean ± SEM; brain n = 15 per probe (E, G, I, and K); brain n = 3 per antibody staining (F, H, J, and L); *p < 0.05; ***p < 0.001; unpaired t test.

(M) Colocalization of myr-DF (non-striped) and Syt1-DF (striped) compartments with markers of the endolysosomal system. Shown are ratios for yellow-fixed and red-fixed terminal hub compartments that colocalize with a given antibody divided by the total number of compartments. The yellow-fixed and red-fixed bars are stacked in the bar chart. Mean ± SEM; *p < 0.05; ***p < 0.001; unpaired t test; brain n = 3–5 per antibody staining. See also Figure S3.

compartments live. We found that compartments of both types exhibited restricted mobility within the axon terminals but continuously exchanged membrane cargo and budded off smaller axon trafficking vesicles; we therefore termed these compartments "hubs" (Figures 3A–3J; Movie S3). Specifically, using resonant confocal microscopy, we could track individual hubs at the axon terminal in 4D with a temporal resolution of 7.5 s over the course of several hours in the case of myr-DF (Figures 3A–3C, 3L, and 3M) but typically only for 15 min in the case of the smaller Syt1-DF hubs (Figures 3F–3H). Hubs marked by either probe were locally restricted with a displacement of maximally 2 μm in 5 min (Figures 3E, 3J, and 3K) and maximally 3 μm over 5 hr for myr-DF (Figure 3L). Analysis of the 4D tracking data revealed, unexpectedly, no unequivocal *de novo* appearance or disappearance of individual hubs. Instead, both myr and Syt1 hubs exhibited frequent and balanced fusion and fission events at a rate of 2/min that resulted in continuous enlargements and splits suggestive of continuous cargo flux (Figures 3N and 3O; Table S1; Movie S3).

The budding of smaller vesicles that entered the axon for retrograde trafficking was more frequent for Syt1-DF than for myr-DF (Figures 3A, 3B, 3F, and 3G). Similar to the hubs, the axonal trafficking vesicles were exclusively red live for both probes (Figures 3H, S4A, and S4B; Movie S3). Larger axonal vesicles moved predominantly retrogradely, whereas the smallest discernible axonal vesicles moved in both directions (Figures S4A–S4F). To quantitatively analyze the net movements of axonal trafficking vesicles, we computed Markov state models. Both myr-DF- and Syt1-DF-positive axonal trafficking vesicles exhibited increasing "committor probabilities" toward the cell body, which indicate net retrograde trafficking back to the cell body (Figures 3D and 3I).

To compare the dynamics of hubs and axonal trafficking vesicles with autophagosomes, we co-expressed the autophagosome marker Atg8-mCherry with myr-GFP or Syt1-GFP. Consistent with the colocalization in fixed preparations, live imaging of these two pairs revealed that small subsets of myr-DF and (to a lesser extent) Syt1-DF indeed mark autophagosomes (Figures S4G–S4I). However, Atg8-positive autophagosomes exhibited very different dynamics compared to hub compartments: they (1) form *de novo* at axon terminals (controlled for z movement in 4D data; Movie S4) and exhibit (2) significantly lower fission/fusion rates (Figure S4J); (3) a size distribution distinct from

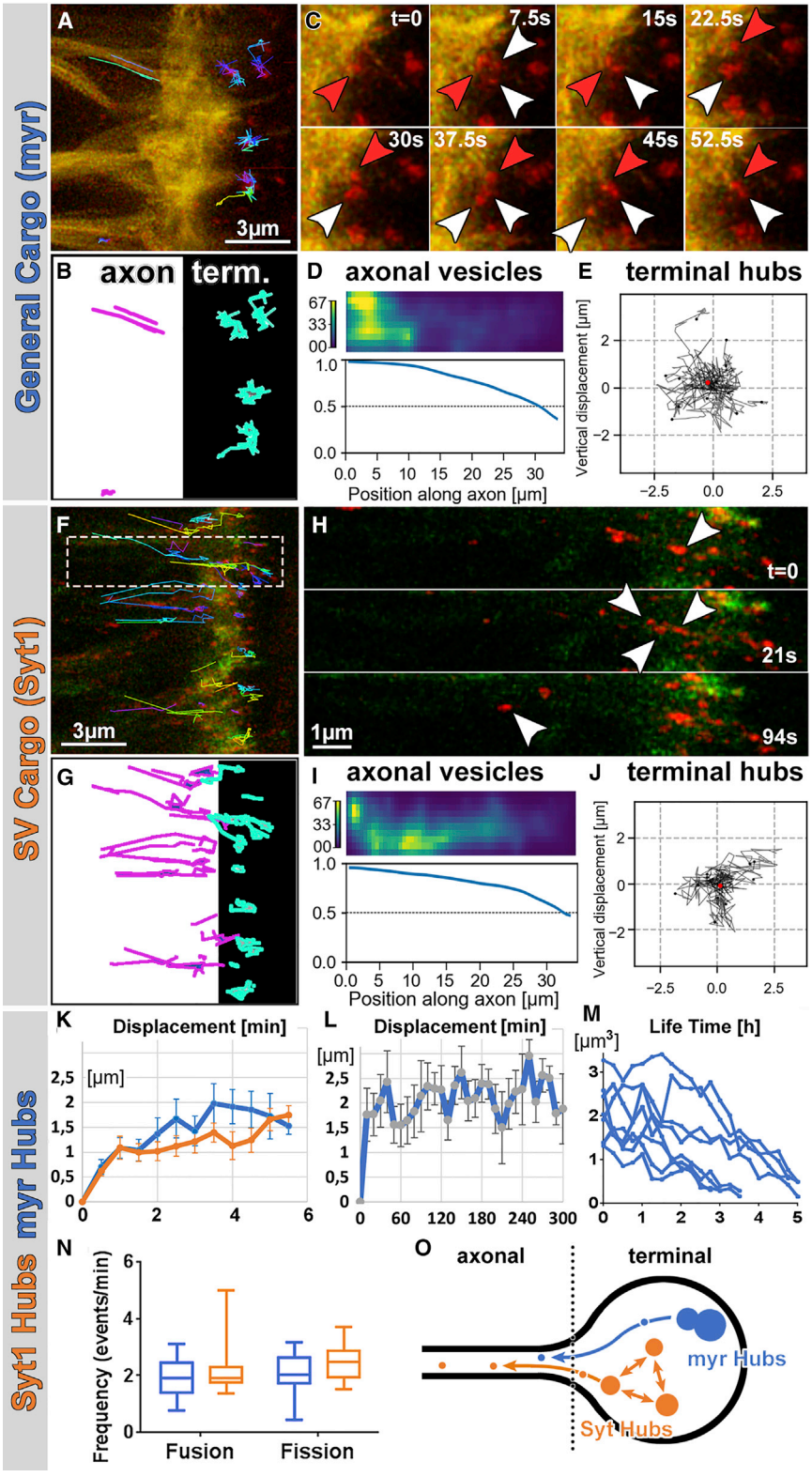

Figure 3. The Hub Compartments: Continuous Flux through Fusion, Fission, and Budding of Retrograde Trafficking Vesicles

(A, B, F, and G) 4D tracking of acidified compartments marked by myr-DF (A and B) and Syt1-DF (F and G) revealed distinct terminal hub compartments and retrogradely trafficking axonal vesicles.

(C) myr-DF-positive hubs undergo multiple fusion (red arrowheads) and fission (white arrowheads) events in seconds.

(D and I) Markov state models of axonal vesicles for myr-DF (hub n = 222; D) and Syt1-DF (hub n = 202; I) revealed high probabilities for trafficking toward the cell body (to the left) and increasing "committor probabilities" along the axon.

(E and J) Trajectories from origin of myr-DF (hub n = 12; E) and Syt1-DF (hub n = 11; J) hubs with mean displacement revealed no directed movements of hub compartments. Red dot indicates the origin of movement.

(H) Example of Syt1-DF hub compartment fission into multiple compartments, including retrograde axonal trafficking vesicle (arrowhead).

(K) Mean ± SEM displacement from origin of myr or Syt1 hubs in 6 min. Mean ± SEM; hub n = 11 per probe.

(L) Mean ± SEM displacement from origin of myr hubs over 5 hr (hub n = 9).

(M) Lifetime of myr hubs represented as volume of hubs over hours (hub n = 8).

(N) Fusion and fission frequencies of myr and Syt1 hubs. Box and whiskers plot shows 5–95 percentiles; hub n = 12–15 per probe.

(O) Schematic of hub compartment dynamics: no *de novo* appearance or disappearance but continuous flux and budding for retrograde trafficking.

See also Figure S4, Table S1, and Movies S3 and S4.

both myr-DF- and Syt1-DF-degradative compartments (Figure S4K); and (4) no budding of axonal trafficking vesicles. Most importantly, in contrast to the Syt1- and myr-containing hubs, Atg8-positive autophagosomes entered the axon directly (Movie S4). We conclude that autophagosomes are largely distinct from endolysosomal hub compartments at axon terminals.

In sum, live imaging revealed flux within a network of continuously splitting and fusing endolysosomal hubs that do not leave the axon terminals, whereas smaller, retrogradely trafficking axonal vesicles provide an exit from this "hub flux" at varying stages of endolysosomal maturity (Figures 2M and 3O; Movie S3).

Two Distinct Pools of Hub Compartments

We next probed the cargo specificity of the hubs marked by our cargo probes. Co-labeling of axon terminal hubs marked by myr-DF and Syt1-DF with a panel of SV and plasma membrane protein antibodies revealed a remarkably clear separation of markers: SV proteins, most prominently Rab3 and CSP, exhibited 6- to 8-fold more colocalization with Syt1-DF compared to myr-DF. In contrast, the t-SNARE Syx1A

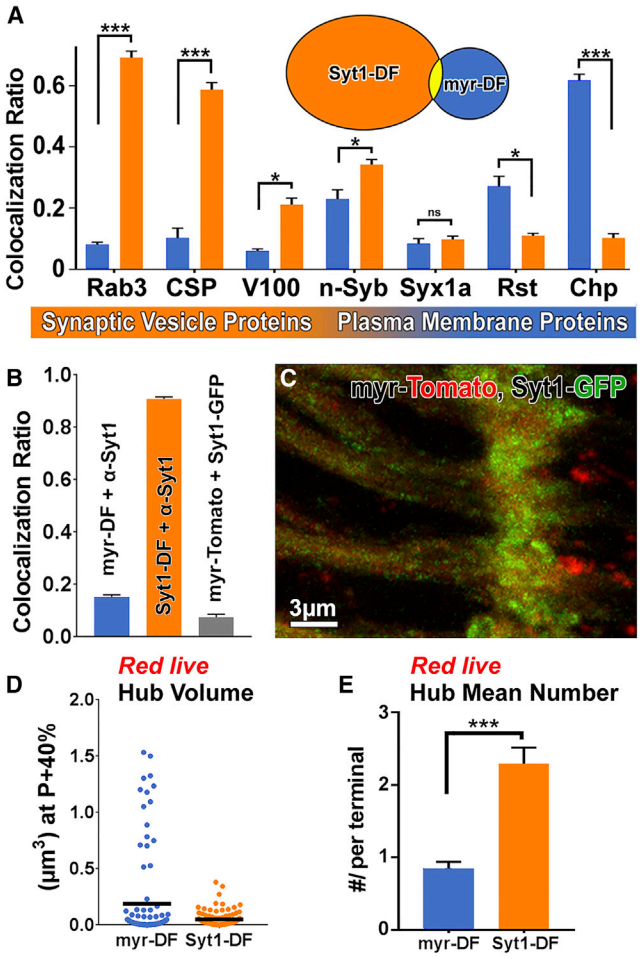

Figure 4. Two Distinct Pools of Hub Compartments

(A) Colocalization ratios of myr-DF- (blue) and Syt1-DF (orange)-marked compartments with antibody labeling against SV and plasma membrane proteins in fixed preparations reveals largely distinct compartment pools. Mean ± SEM; *p < 0.05; ***p < 0.001; unpaired t test; brain n = 3 per antibody staining.

(B) Colocalization ratios of myr-DF with anti-Syt1, Syt1-DF with anti-Syt1, and myr-Tomato with Syt-GFP. Mean ± SEM; brain n = 3 per colocalization.

(C) Co-expression of myr-Tomato and Syt1-GFP reveals distinct compartments.

(D) Volumes of acidified (red) compartments at axon terminals. Hub n = 100 per probe; black lines indicate mean values.

(E) Mean number of acidified compartments per axon terminal at P+40%. Mean ± SEM; ***p < 0.001; unpaired t test; brain n = 3–5 per probe.

See also Figure S5.

colocalized at low levels with both types and the non-SV plasma membrane receptors Rst and Chp colocalized 3–6 times more with myr-DF (Figures 4A, S5A, and S5B). Immunolabeling for Syt1 marked almost all Syt1-DF compartments but only 15% of myr-DF compartments (Figure 4B), indicating that most myr-DF compartments do not contain Syt1. Indeed, live co-expression of myr-Tomato and Syt1-GFP revealed <10% colocalization (Figures 4B and 4C). Quantitative analysis of the red-live axon terminal hubs marked by Syt1-DF revealed 2.5 times more compartments that were on average half the size compared to those marked by myr-DF (Figures 4D and 4E). These data indicate that myr-DF and Syt1-DF mark distinct pools of hub compartments at axon terminals. SV-specific hubs mostly exclude plasma membrane proteins.

Distinct Molecular Mechanisms Sort and Degrade Plasma Membrane Proteins and SV Proteins

As reported above, Rab7 (canonical endolysosomal degradation and autophagy) and Atg8 (autophagy) exhibited significantly increased colocalization with the plasma membrane hubs compared to SV hubs (Figure 2M). In contrast, n-Syb and V100 (NSD) exhibited increased colocalization with SV hubs compared to plasma membrane hubs (Figure 4A). These findings prompted us to probe the functional roles of Rab7, n-Syb, and V100 in the sorting and degradation of the distinct hubs. *rab7* is a ubiquitous key factor required for maturation in the endolysosomal system [38] and at least some types of autophagy [40] and the gene underlying the neuropathy Charcot-Marie-Tooth 2B [17, 23]. The vesicular ATPase component V100 and the vesicle SNARE neuronal synaptobrevin (n-Syb) are both exclusive neuronal proteins that were initially identified as SV proteins with single neuronal orthologs from worms to humans [41, 42]. In flies, V100 and n-Syb function in endolysosomal degradation, and it is this second function that leads to photoreceptor adult-onset degeneration in the mutants [20, 22]. We have previously proposed the term neuronal sort-and-degrade (NSD) for this putative neuronal branch of the endolysosomal system. The neuron-specific functions and cargo specificity of both canonical endolysosomal degradation and NSD have so far remained unknown.

To analyze cell-autonomous, cargo-specific sorting and degradation in mutant neurons, we performed live imaging in mosaic brains in which only a subset of photoreceptor neurons was mutant for *rab7*, *v100*, or *n-syb* in otherwise wild-type brains (Figures 5A–5H). In all three mutants, hub compartments were present at axon terminals, with one exception: myr-DF hub compartments were lost at axon terminals of *rab7* mutant neurons (Figures 5C and 5I). In contrast, Syt1-DF hub compartment numbers were unaltered in the *rab7* mutant and instead significantly decreased in both NSD mutants. Fusion and fission rates between hub compartments were not significantly changed for either probe in NSD mutants and equally reduced for the Syt1-DF probe and hence not likely to be contributors to the changes in hub numbers (Table S1). These surprising observations suggest that the normal formation of hub compartments containing SV cargo requires NSD but is *rab7* independent, whereas the formation of myr-DF hub compartments is *rab7* dependent but NSD independent.

To further test the cargo specificity of the two molecular mechanisms, we overexpressed *rab7*, *v100*, and *n-syb* in the presence of both probes. Overexpression of *rab7* had no significant effect on either compartment type. However, overexpression of *v100* or *n-syb* selectively affected Syt1-DF hub compartments in a manner opposite to their loss of function. myr-DF hub compartments were not affected by either NSD mutant, similar to their loss of function (Figures S6A and S6B). Finally, n-Syb knockdown in the *v100* mutant background further decreased the number of SV hubs, but not myr-DF hubs (Figures 5B, 5F, 5H, 5I, and S6C–S6J), suggesting additive cell biological functions of V100 and n-Syb that are specific to SV hubs.

Next, we assayed endolysosomal progression of both probes from early via late endosomes to lysosomes using Rab5, Rab7,

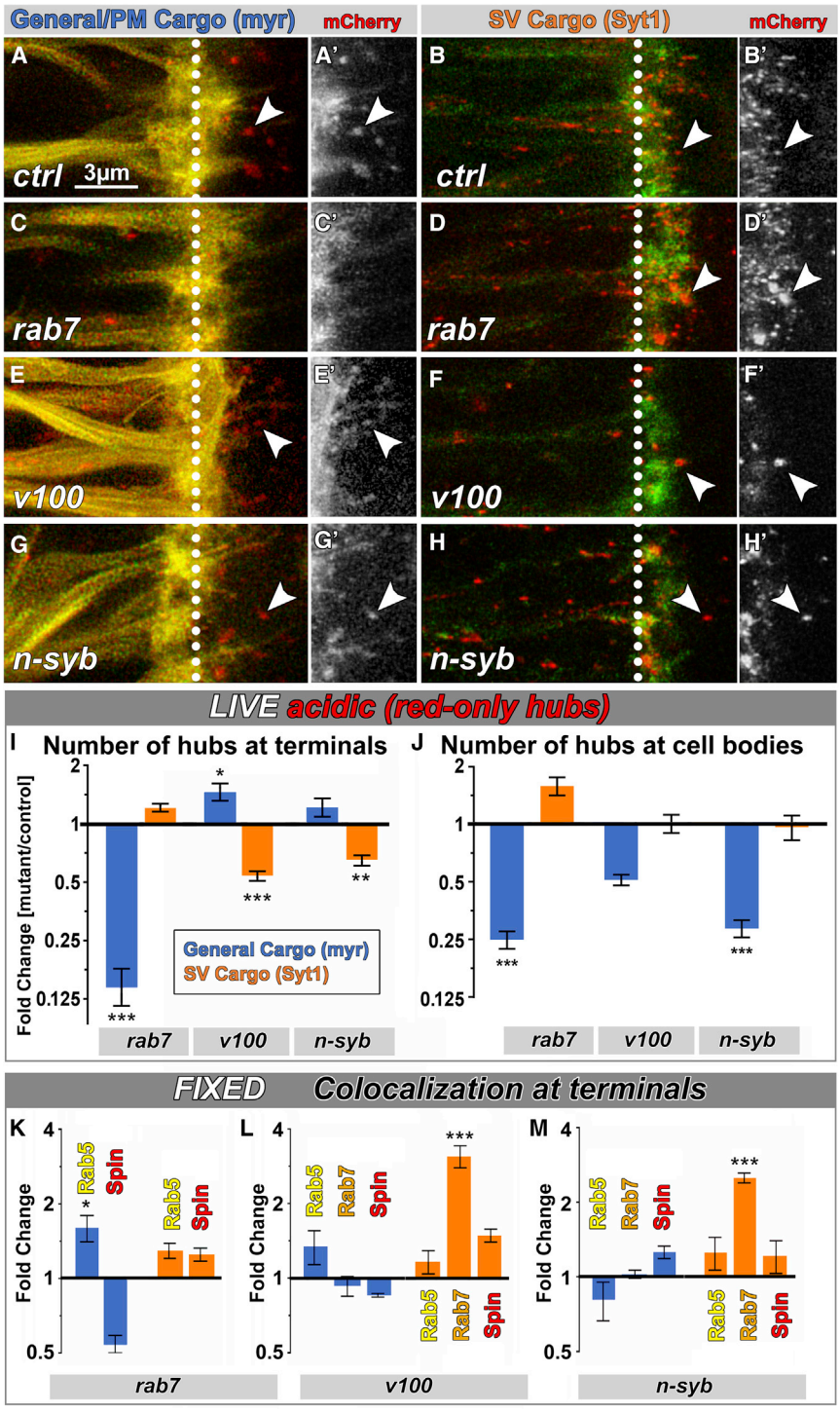

Figure 5. Distinct Molecular Mechanisms Sort and Degrade Plasma Membrane Proteins and SV Proteins

(A–H′) Live imaging of myr-DF and Syt1-DF in wild-type (A–B′), *rab7* (C–D′), *v100* (E–F′), or *nsyb* (G–H′) mutant background in P+40% photoreceptor axon terminals. Arrowheads, examples of acidic (red-only live) compartments at axon terminals. White dotted lines mark the boundaries between axon (left) and axon terminals (right).

(I and J) Relative number of degradative compartments in mutants from live-imaging data in axon terminals (I) and cell bodies (J). Mean ± SEM; *p < 0.05; **p < 0.01; ***p < 0.001; unpaired t test; brain n = 4–8 per experimental condition.

(K–M) Relative colocalization ratio changes of yellow-fixed compartments with early endosomes (Rab5), late endosomes (Rab7), and lysosomes (Spin) in *rab7* (K), *v100* (L), and *nSyb* (M) mutant axon terminals. Mean ± SEM; *p < 0.05; ***p < 0.001; brain n = 3 per experimental condition; unpaired t test.

See also Figure S6.

and Spin co-labelings in fixed preparations. As shown in Figure 5K, loss of *rab7* leads to an increase of myr-DF in Rab5-positive compartments and a corresponding reduction in lysosomal compartments, consistent with the known role of Rab7 in endosomal maturation. In contrast, Syt1-DF exhibited no such changes in the *rab7* mutant, corroborating that sorting of Syt1-DF into SV hubs at axon terminals is *rab7* independent (Figure 5K). The opposite cargo specificity was observed in the two NSD mutants *v100* and *n-syb*: whereas myr-DF exhibited no significant alterations in either NSD mutant, the Syt1-DF probe accumulated 3-fold in late endosomal (Rab7-positive) compartments in both NSD mutants (Figures 5L and 5M), suggesting that degradation of Syt1-DF, but not myr-DF, is NSD dependent. Note that Syt1-DF accumulates in a Rab7-positive compartment, even though sorting and maturation of Syt1-DF are *rab7* independent, consistent with a known further role of Rab7 in lysosomal degradation based on interaction with the homotypic fusion and vacuole protein sorting (HOPS) complex [43]. Indeed, we observed an increase of SV hub volume in the *rab7* mutant (Figure S6K) as well as in a mutant for the HOPS complex component Vps33A/Carnation (*car*) (Figures S6L–S6Q), consistent with impaired degradation. In contrast to rab7, loss of *car* affects both probes similarly, effectively singling out a late common role in degradation with no effects on sorting or maturation of either hub compartments (Figures S6K, S6P, and S6Q). We conclude that sorting of SV cargo depends only on NSD (and is Rab7 independent) and sorting of general plasma membrane cargo depends only on Rab7 (and is NSD independent).

CP1 Is a Protease Specific to SV Hubs

Local degradation requires the delivery of proteases to the hub compartments at axon terminals. In *Drosophila* photoreceptors, the Cathepsin-L-like protease CP1 mediates neurodegeneration

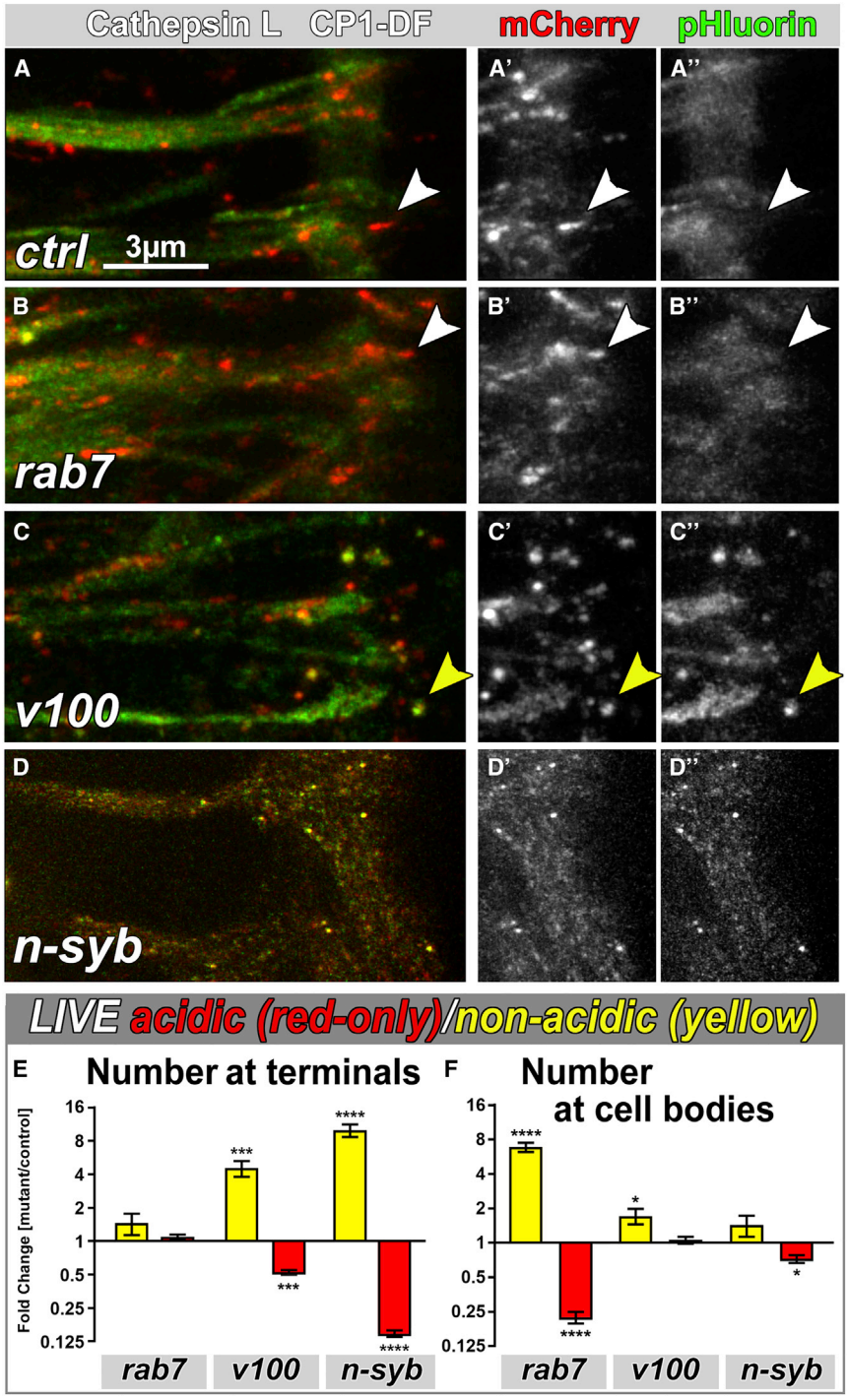

Figure 6. The Cathepsin-L-like Protease CP1 Is Specific to SV Hubs

(A–D′′) Live imaging of CP1-DF in wild-type (A–A′′), *rab7* (B–B′′), *v100* (C–C′′), or *nsyb* (D–D′′) mutant axon terminals. White arrowhead, acidic (red-only live) compartment; yellow arrowhead, non-acidic (yellow live) compartment.

(E and F) Relative number of acidified (red) or non-acidified (yellow) CP1-DF-positive compartments at axon terminals (E) and cell bodies (F). Mean ± SEM; *p < 0.05; ***p < 0.001; ****p < 0.0001; brain n = 3 per experimental condition; unpaired t test. See also Figure S7.

[44]. To test whether CP1 is a protease that functions in one or both types of hub compartments, we generated a CP1-DF probe for live imaging. CP1-DF is incorporated into red-live hub compartments at axon terminals that appear in size and number more similar to Syt1-DF than myr-DF (Figures 6A, S7A, and S7B). Co-labeling of CP1-DF-positive hub compartments with SV and plasma membrane markers in fixed preparations appeared similar to SV hubs (Figures S7C and S5). As shown in Figures 6A–6D, CP1-DF labeling of acidic compartments is selectively affected in the NSD mutants but unaltered in *rab7*. Because there are almost no myr-positive hubs in *rab7* mutant axon terminals, CP1-DF may specifically supply SV hubs. Indeed, in *n-syb* mutant terminals, CP1-DF labeling of acidified compartments is completely lost and CP1-DF appears trapped in numerous non-acidified, smaller vesicles, indicating a complete failure to reach hub compartments (Figures 6D and 6E). In contrast, in the *v100* mutant, CP1-DF does reach hub compartments, but around 50% remain non-acidified, indicating that *v100* is partially required for acidification of SV hubs (Figures 6C, 6E, and S7D). Correspondingly, n-Syb knockdown in the *v100* mutant background caused an additive effect with both the small yellow CP1-delivery vesicles as well as larger non-acidified hubs (Figures S7E–S7I), i.e., a combination of the *nsyb* and *v100* mutant phenotypes (Figure 6). We conclude that CP1 is sorted specifically into hub compartments of the SV pathway at axon terminals via an *n-syb*-dependent and *rab7*-independent mechanism (Figure 7).

Cargo Separation Occurs Specifically at the Axon Terminal and Not in the Cell Body

Finally, we compared the molecularly distinct endolysosomal sorting of plasma membrane and SV cargo between the cell body and the axon terminal. In cell bodies, myr-DF and Syt1-DF colocalized more similarly with all endolysosomal markers (Figure S6R) as well as all SV markers (Figure S6S). Hence, both probes mostly marked common, mixed compartments in the cell body. In contrast to the axon terminal, the NSD mutants *v100* and *n-syb* did not specifically affect SV proteins in the cell body (Figures 5J and S6T). Instead, *v100* and *n-syb* mutants exhibited a reduction in the numbers of myr-DF compartments in the cell body and no changes to compartments containing Syt1-DF (Figure 5J). Also opposite to phenotypes at axon terminals, CP1-DF

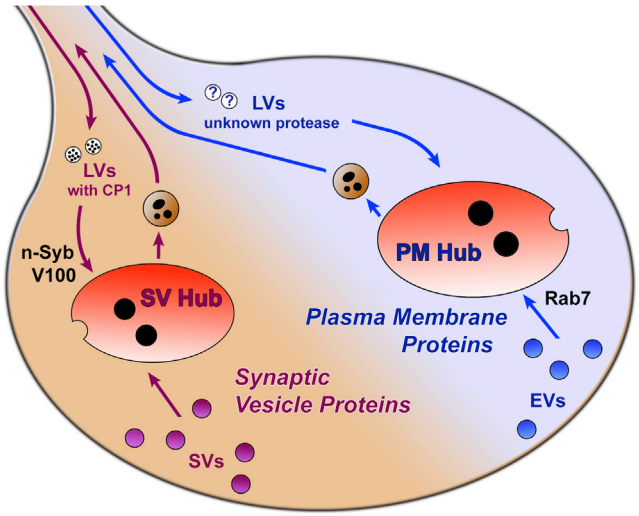

Figure 7. Model: Two Parallel Membrane Degradation Mechanisms at Axon Terminals

Axon terminals harbor at least two types of mostly non-overlapping endolysosomal hub compartments: one for synaptic vesicle (SV) proteins and one for general plasma membrane (PM) proteins. Maturation of SV hubs, but not PM hubs, depends on the n-Syb-dependent delivery of the protease CP1 and acidification by neuronal vATPase component V100. Maturation of PM hubs, but not SV hubs, depends on the small Rab7 GTPase. EVs, endosomal vesicles; LVs, lysosomal vesicles.

accumulated in non-acidified compartments in cell bodies mutant for *rab7*, but not *v100* and *n-syb* (Figures 6E, 6F, and S7J). We conclude that the *rab7*- and NSD-dependent mechanisms sort and degrade in a cargo-specific manner exclusively at the axon terminal. In contrast, the same molecules that function in separate pathways at axon terminals are found in mixed membrane degradation compartments in the cell bodies of the same neuron (Figures S6R, S6S, and S7K). Hence, sorting of SV proteins and plasma membrane proteins for degradation in separate endolysosomal pathways occurs locally at axon terminals (Figure 7).

DISCUSSION

In this study, we investigated neuronal membrane protein degradation *in vivo* from the perspective of different cargo probes and unbiased with respect to sorting and degradation mechanisms. Our key findings are (1) the direct live observation of membrane protein degradation at axon terminals in large, acidified hubs: acidic, degradative endolysosomal compartments that undergo continuous flux and bud of retrograde transport vesicles and (2) the cargo-specific sorting of SV and plasma membrane proteins into different hubs via two molecularly distinct pathways at axon terminals.

"Hub Flux" and Membrane Protein Turnover

It is surprising that the only clearly discernible compartments at axon terminals are red live, large, acidified, and spatiotemporally relatively stable endolysosomal compartments. We named these compartments hubs because of their continuous fission, fusion, and budding of smaller retrograde trafficking vesicles. We never observed appearance or disappearance of an entire hub but only the formation of hubs by fusion of several smaller vesicles and splitting into multiple smaller compartments that underwent renewed cycles of fusion. These dynamics are reflected in hub composition and maturation: at any point in time, some hubs are marked by early endosomal markers and contain undegraded probes, whereas others are marked by lysosomal markers and contain partially degraded probes.

How does this "hub flux" contribute to the sorting and degradation of dysfunctional membrane proteins? A key insight comes from the characterization of retrograde trafficking vesicles: the axonal vesicles exhibit the same composition and a mix of early and late markers and degraded and undegraded probes. These observations are most straightforwardly explained with random mixing of hubs and random budding of axonal vesicles, irrespective of their maturation stage. In this model, sorting into hubs carries a probabilistic chance of degradation that increases with time (either in hubs or in retrograde trafficking vesicles). Sorting into hubs ensures degradation if membrane proteins cannot be recycled back into the axon terminal; alternatively, degradation and recycling may both be probabilistic. The latter would imply that not only dysfunctional proteins are sorted into hubs. Both mechanisms could ensure a pool of functional synaptic proteins that increases with the amount of endolysosomal flux, as previously observed for the Skywalker/Rab35 mechanism [12, 19].

How SV membrane proteins are specifically sorted into SV hubs is unclear. Because sorting of Syt1-DF into SV hubs is Rab7 independent, SV hub maturation bypasses the requirement for Rab5-to-Rab7 conversion [39]. Neither n-Syb (a vesicle SNARE and membrane fusion factor) nor V100 (part of a proton pump) are required for the continuous fusion and fission of SV hubs. However, the reduced axon terminal numbers of SV hubs are consistent with roles in the sorting of SVs to SV hubs. Different SV retrieval mechanisms, including ultrafast endocytosis, clathrin-mediated endocytosis, and bulk endocytosis [45, 46], may account for different mechanisms and routes to local degradative hubs. Preassembled plasma membrane cargo complexes may play a role in promoting the different endocytic routes [46]. Our colocalization measurements revealed a distinction between two membrane degradation mechanisms with enrichments of SV proteins versus plasma membrane proteins between 3- and 8-fold, but not a 100% separation. Hence, if protein complexes facilitate sorting into a specific endocytic pathway or hub compartments, they may do so in a probabilistic fashion.

Continuous flux is a hallmark of endolysosomal compartments and results in low colocalization ratios with dynamically changing molecular markers and difficulties to unambiguously identify a specific compartment at any point in time. Our live observation of dynamic hubs as sorting and degradation stations at axon terminals was only made possible by their integrity over time and may provide an inroad to the study of distinct, cargo-specific mechanisms that keep neurons and their synaptic terminals functional.

Hubs in the Context of Known Membrane Sorting and Degradation Mechanisms

We observed constitutive turnover of SV hubs prior to synaptogenesis and neuronal activity. In contrast, previous work on SV

"rejuvenation" focused on turnover that increases in response to neuronal activity [12, 19]. Colocalization of axon terminal hubs with the Rab35 GAP Skywalker (Sky) revealed equal overlap with both hub types. This could indicate an intersection of different endolysosomal pathways; alternatively, Sky may only temporarily localize to hubs depending on their maturation stage. We favor the second possibility, because the early endosomal Rab5 and the lysosomal marker Spin exhibit similar colocalization ratios and all known endolysosomal markers depend in some way on the maturation stage [38, 47]. Our colocalization implies Sky in both the canonical and SV pathway. Consistent with this, *rab7* affects Sky-dependent rejuvenation and the *sky* mutant affects the turnover of an n-Syb imaging probe [11].

Autophagy similarly intersects with axon terminal hub compartments based on colocalization with Atg8, albeit this colocalization is significantly higher for the *rab7*-dependent general PM hubs than for the SV hubs. However, the hubs and axonal trafficking vesicles are distinct from autophagosomes based on their dynamics: Atg8-positive compartments are not part of the "hub flux," emerge *de novo*, and directly enter the axon without prior fission. It is possible that autophagosomes can engulf hub compartments and thus provide an alternative degradative exit to budding of retrograde trafficking vesicles. A Rab26-dependent mechanism was recently proposed for the sorting of SVs to pre-autophagosomal compartments prior to Atg8 recruitment, which may represent a similar hub compartment [48].

Cathepsin L: A Protease with Cargo Specificity

In this study, we showed that cathepsin-L-like protease CP1 has specificity for the SV hubs at axon terminals. This finding is consistent with several cystein cathepsins that have been characterized for their tissue-specific expression [49]. In mammalian systems, cathepsin L selectively degrades polyglutamine (polyQ)-containing proteins, but not other types of aggregation-prone proteins lacking polyQ [50]. In HeLa and Huh-7 cells, cathepsin L was reported to degrade autophagosomal membrane markers, but not proteins in the lumen of autophagosomes [51]. In contrast, the major histocompatibility complex (MHC) class-II-associated invariant chain is specifically degraded by cathepsin S, but not cathepsin L, in $CD4^+$ T cells [52]. Our characterization of cargo-specific membrane degradation machinery with a specific protease raises the question to what extent different membrane degradation mechanisms are characterized and may require specific proteases.

STAR★METHODS

Detailed methods are provided in the online version of this paper and include the following:

- KEY RESOURCES TABLE
- CONTACT FOR REAGENT AND RESOURCE SHARING
- EXPERIMENTAL MODEL AND SUBJECT DETAILS
  - Fly husbandry
  - Flies
- METHOD DETAILS
  - Brain culture and live imaging
  - Immunohistochemistry
  - Image processing
  - Electroretinogram (ERG) Recordings
- QUANTIFICATION AND STATISTICAL ANALYSIS
  - Quantification and Statistical Analysis
  - Markov State Modeling

SUPPLEMENTAL INFORMATION

Supplemental Information includes seven figures, one table, and four movies and can be found with this article online at https://doi.org/10.1016/j.cub.2018.02.032.

ACKNOWLEDGMENTS

We would like to thank all members of the Hiesinger lab, Volker Haucke, Bettina Winckler, Mathias Wernet, Bassem Hassan, Ilya Bezprozvanny, Craig Garner, and Stephan Sigrist for helpful discussions. We further thank Patrik Verstreken, Sergio Grinstein, Helmut Kramer, and the Bloomington Stock Center in Indiana for reagents. This work was supported by the Deutsche Forschungsgemeinschaft (SFB958 and SFB/TRR186), NeuroCure Cluster Berlin, NIH (RO1EY018884 and RO1EY023333), and Muscular Dystrophy Association of the USA to P.R.H. E.J.J. was supported by the NIH (T32 NS069562 and F31 NS084774) and DFG (SFB958).

AUTHOR CONTRIBUTIONS

E.J.J., F.R.K., M.N.O., and P.R.H. designed the experiments and wrote the paper. L.S.B., D.E., and H.W. helped with experiments and data analysis. M.O. and S.P. provided the Markov state model analyses.

DECLARATION OF INTERESTS

The authors declare no competing interests.

Received: October 3, 2017
Revised: January 24, 2018
Accepted: February 14, 2018
Published: March 15, 2018

REFERENCES

1. Arendt, T. (2009). Synaptic degeneration in Alzheimer's disease. Acta Neuropathol. *118*, 167–179.
2. Shankar, G.M., and Walsh, D.M. (2009). Alzheimer's disease: synaptic dysfunction and Abeta. Mol. Neurodegener. *4*, 48.
3. Wong, E., and Cuervo, A.M. (2010). Autophagy gone awry in neurodegenerative diseases. Nat. Neurosci. *13*, 805–811.
4. Morales, I., Sanchez, A., Rodriguez-Sabate, C., and Rodriguez, M. (2015). The degeneration of dopaminergic synapses in Parkinson's disease: a selective animal model. Behav. Brain Res. *289*, 19–28.
5. Bezprozvanny, I., and Hiesinger, P.R. (2013). The synaptic maintenance problem: membrane recycling, Ca2+ homeostasis and late onset degeneration. Mol. Neurodegener. *8*, 23.
6. Wang, Y.C., Lauwers, E., and Verstreken, P. (2017). Presynaptic protein homeostasis and neuronal function. Curr. Opin. Genet. Dev. *44*, 38–46.
7. Maday, S., and Holzbaur, E.L. (2012). Autophagosome assembly and cargo capture in the distal axon. Autophagy *8*, 858–860.
8. Maday, S., and Holzbaur, E.L. (2014). Autophagosome biogenesis in primary neurons follows an ordered and spatially regulated pathway. Dev. Cell *30*, 71–85.
9. Maday, S., and Holzbaur, E.L. (2016). Compartment-specific regulation of autophagy in primary neurons. J. Neurosci. *36*, 5933–5945.
10. Maday, S., Wallace, K.E., and Holzbaur, E.L. (2012). Autophagosomes initiate distally and mature during transport toward the cell soma in primary neurons. J. Cell Biol. *196*, 407–417.

11. Fernandes, A.C., Uytterhoeven, V., Kuenen, S., Wang, Y.C., Slabbaert, J.R., Swerts, J., Kasprowicz, J., Aerts, S., and Verstreken, P. (2014). Reduced synaptic vesicle protein degradation at lysosomes curbs TBC1D24/sky-induced neurodegeneration. J. Cell Biol. *207*, 453–462.

12. Uytterhoeven, V., Kuenen, S., Kasprowicz, J., Miskiewicz, K., and Verstreken, P. (2011). Loss of skywalker reveals synaptic endosomes as sorting stations for synaptic vesicle proteins. Cell *145*, 117–132.

13. Wang, D., Chan, C.C., Cherry, S., and Hiesinger, P.R. (2013). Membrane trafficking in neuronal maintenance and degeneration. Cell. Mol. Life Sci. *70*, 2919–2934.

14. Cai, Q., Lu, L., Tian, J.H., Zhu, Y.B., Qiao, H., and Sheng, Z.H. (2010). Snapin-regulated late endosomal transport is critical for efficient autophagy-lysosomal function in neurons. Neuron *68*, 73–86.

15. Lloyd, T.E., Machamer, J., O'Hara, K., Kim, J.H., Collins, S.E., Wong, M.Y., Sahin, B., Imlach, W., Yang, Y., Levitan, E.S., et al. (2012). The p150(Glued) CAP-Gly domain regulates initiation of retrograde transport at synaptic termini. Neuron *74*, 344–360.

16. Jin, E.J., Kiral, F.R., and Hiesinger, P.R. (2017). The where, what, and when of membrane protein degradation in neurons. Dev. Neurobiol. Published online September 7, 2018. https://doi.org/10.1002/dneu.22534.

17. Cherry, S., Jin, E.J., Ozel, M.N., Lu, Z., Agi, E., Wang, D., Jung, W.H., Epstein, D., Meinertzhagen, I.A., Chan, C.C., and Hiesinger, P.R. (2013). Charcot-Marie-Tooth 2B mutations in rab7 cause dosage-dependent neurodegeneration due to partial loss of function. eLife *2*, e01064.

18. Deinhardt, K., Salinas, S., Verastegui, C., Watson, R., Worth, D., Hanrahan, S., Bucci, C., and Schiavo, G. (2006). Rab5 and Rab7 control endocytic sorting along the axonal retrograde transport pathway. Neuron *52*, 293–305.

19. Sheehan, P., Zhu, M., Beskow, A., Vollmer, C., and Waites, C.L. (2016). Activity-dependent degradation of synaptic vesicle proteins requires Rab35 and the ESCRT pathway. J. Neurosci. *36*, 8668–8686.

20. Williamson, W.R., Wang, D., Haberman, A.S., and Hiesinger, P.R. (2010). A dual function of V0-ATPase a1 provides an endolysosomal degradation mechanism in Drosophila melanogaster photoreceptors. J. Cell Biol. *189*, 885–899.

21. Williamson, W.R., Yang, T., Terman, J.R., and Hiesinger, P.R. (2010). Guidance receptor degradation is required for neuronal connectivity in the Drosophila nervous system. PLoS Biol. *8*, e1000553.

22. Haberman, A., Williamson, W.R., Epstein, D., Wang, D., Rina, S., Meinertzhagen, I.A., and Hiesinger, P.R. (2012). The synaptic vesicle SNARE neuronal Synaptobrevin promotes endolysosomal degradation and prevents neurodegeneration. J. Cell Biol. *196*, 261–276.

23. Verhoeven, K., De Jonghe, P., Coen, K., Verpoorten, N., Auer-Grumbach, M., Kwon, J.M., FitzPatrick, D., Schmedding, E., De Vriendt, E., Jacobs, A., et al. (2003). Mutations in the small GTP-ase late endosomal protein RAB7 cause Charcot-Marie-Tooth type 2B neuropathy. Am. J. Hum. Genet. *72*, 722–727.

24. Hara, T., Nakamura, K., Matsui, M., Yamamoto, A., Nakahara, Y., Suzuki-Migishima, R., Yokoyama, M., Mishima, K., Saito, I., Okano, H., and Mizushima, N. (2006). Suppression of basal autophagy in neural cells causes neurodegenerative disease in mice. Nature *441*, 885–889.

25. Komatsu, M., Waguri, S., Chiba, T., Murata, S., Iwata, J., Tanida, I., Ueno, T., Koike, M., Uchiyama, Y., Kominami, E., and Tanaka, K. (2006). Loss of autophagy in the central nervous system causes neurodegeneration in mice. Nature *441*, 880–884.

26. Vanhauwaert, R., Kuenen, S., Masius, R., Bademosi, A., Manetsberger, J., Schoovaerts, N., Bounti, L., Gontcharenko, S., Swerts, J., Vilain, S., et al. (2017). The SAC1 domain in synaptojanin is required for autophagosome maturation at presynaptic terminals. EMBO J. *36*, 1392–1411.

27. Okerlund, N.D., Schneider, K., Leal-Ortiz, S., Montenegro-Venegas, C., Kim, S.A., Garner, L.C., Gundelfinger, E.D., Reimer, R.J., and Garner, C.C. (2017). Bassoon controls presynaptic autophagy through Atg5. Neuron *93*, 897–913.e7.

28. Goo, M.S., Sancho, L., Slepak, N., Boassa, D., Deerinck, T.J., Ellisman, M.H., Bloodgood, B.L., and Patrick, G.N. (2017). Activity-dependent trafficking of lysosomes in dendrites and dendritic spines. J. Cell Biol. *216*, 2499–2513.

29. Özel, M.N., Langen, M., Hassan, B.A., and Hiesinger, P.R. (2015). Filopodial dynamics and growth cone stabilization in Drosophila visual circuit development. eLife *4*, e10721.

30. Prosser, D.C., Whitworth, K., and Wendland, B. (2010). Quantitative analysis of endocytosis with cytoplasmic pHluorin chimeras. Traffic *11*, 1141–1150.

31. Filimonenko, M., Stuffers, S., Raiborg, C., Yamamoto, A., Malerød, L., Fisher, E.M., Isaacs, A., Brech, A., Stenmark, H., and Simonsen, A. (2007). Functional multivesicular bodies are required for autophagic clearance of protein aggregates associated with neurodegenerative disease. J. Cell Biol. *179*, 485–500.

32. Brose, N., Petrenko, A.G., Südhof, T.C., and Jahn, R. (1992). Synaptotagmin: a calcium sensor on the synaptic vesicle surface. Science *256*, 1021–1025.

33. Han, W., Rhee, J.S., Maximov, A., Lin, W., Hammer, R.E., Rosenmund, C., and Südhof, T.C. (2005). C-terminal ECFP fusion impairs synaptotagmin 1 function: crowding out synaptotagmin 1. J. Biol. Chem. *280*, 5089–5100.

34. Kavalali, E.T., and Jorgensen, E.M. (2014). Visualizing presynaptic function. Nat. Neurosci. *17*, 10–16.

35. Stowers, R.S., and Schwarz, T.L. (1999). A genetic method for generating Drosophila eyes composed exclusively of mitotic clones of a single genotype. Genetics *152*, 1631–1639.

36. Chan, C.C., Scoggin, S., Wang, D., Cherry, S., Dembo, T., Greenberg, B., Jin, E.J., Kuey, C., Lopez, A., Mehta, S.Q., et al. (2011). Systematic discovery of Rab GTPases with synaptic functions in Drosophila. Curr. Biol. *21*, 1704–1715.

37. Sweeney, S.T., and Davis, G.W. (2002). Unrestricted synaptic growth in spinster-a late endosomal protein implicated in TGF-beta-mediated synaptic growth regulation. Neuron *36*, 403–416.

38. Huotari, J., and Helenius, A. (2011). Endosome maturation. EMBO J. *30*, 3481–3500.

39. Rink, J., Ghigo, E., Kalaidzidis, Y., and Zerial, M. (2005). Rab conversion as a mechanism of progression from early to late endosomes. Cell *122*, 735–749.

40. Jäger, S., Bucci, C., Tanida, I., Ueno, T., Kominami, E., Saftig, P., and Eskelinen, E.L. (2004). Role for Rab7 in maturation of late autophagic vacuoles. J. Cell Sci. *117*, 4837–4848.

41. Perin, M.S., Fried, V.A., Stone, D.K., Xie, X.S., and Südhof, T.C. (1991). Structure of the 116-kDa polypeptide of the clathrin-coated vesicle/synaptic vesicle proton pump. J. Biol. Chem. *266*, 3877–3881.

42. Schoch, S., Deák, F., Königstorfer, A., Mozhayeva, M., Sara, Y., Südhof, T.C., and Kavalali, E.T. (2001). SNARE function analyzed in synaptobrevin/VAMP knockout mice. Science *294*, 1117–1122.

43. Balderhaar, H.J., and Ungermann, C. (2013). CORVET and HOPS tethering complexes - coordinators of endosome and lysosome fusion. J. Cell Sci. *126*, 1307–1316.

44. Kinser, R.D., and Dolph, P.J. (2012). Cathepsin proteases mediate photoreceptor cell degeneration in Drosophila. Neurobiol. Dis. *46*, 655–662.

45. Kononenko, N.L., Puchkov, D., Classen, G.A., Walter, A.M., Pechstein, A., Sawade, L., Kaempf, N., Trimbuch, T., Lorenz, D., Rosenmund, C., et al. (2014). Clathrin/AP-2 mediate synaptic vesicle reformation from endosome-like vacuoles but are not essential for membrane retrieval at central synapses. Neuron *82*, 981–988.

46. Cousin, M.A. (2017). Integration of synaptic vesicle cargo retrieval with endocytosis at central nerve terminals. Front. Cell. Neurosci. *11*, 234.

47. Hyttinen, J.M., Niittykoski, M., Salminen, A., and Kaarniranta, K. (2013). Maturation of autophagosomes and endosomes: a key role for Rab7. Biochim. Biophys. Acta *1833*, 503–510.

48. Binotti, B., Pavlos, N.J., Riedel, D., Wenzel, D., Vorbrüggen, G., Schalk, A.M., Kühnel, K., Boyken, J., Erck, C., Martens, H., et al. (2015). The GTPase Rab26 links synaptic vesicles to the autophagy pathway. eLife *4*, e05597.

49. Turk, V., Stoka, V., Vasiljeva, O., Renko, M., Sun, T., Turk, B., and Turk, D. (2012). Cysteine cathepsins: from structure, function and regulation to new frontiers. Biochim. Biophys. Acta *1824*, 68–88.

50. Bhutani, N., Piccirillo, R., Hourez, R., Venkatraman, P., and Goldberg, A.L. (2012). Cathepsins L and Z are critical in degrading polyglutamine-containing proteins within lysosomes. J. Biol. Chem. *287*, 17471–17482.

51. Ueno, T., and Takahashi, K. (2009). A cathepsin L-specific inhibitor preferentially inhibits degradation of autophagosomal LC3 and GABARAP in HeLa and Huh-7 cells. Autophagy *5*, 878–879.

52. Bania, J., Gatti, E., Lelouard, H., David, A., Cappello, F., Weber, E., Camosseto, V., and Pierre, P. (2003). Human cathepsin S, but not cathepsin L, degrades efficiently MHC class II-associated invariant chain in nonprofessional APCs. Proc. Natl. Acad. Sci. USA *100*, 6664–6669.

53. Chinchore, Y., Mitra, A., and Dolph, P.J. (2009). Accumulation of rhodopsin in late endosomes triggers photoreceptor cell degeneration. PLoS Genet. *5*, e1000377.

54. Graf, E.R., Daniels, R.W., Burgess, R.W., Schwarz, T.L., and DiAntonio, A. (2009). Rab3 dynamically controls protein composition at active zones. Neuron *64*, 663–677.

55. Hiesinger, P.R., Fayyazuddin, A., Mehta, S.Q., Rosenmund, T., Schulze, K.L., Zhai, R.G., Verstreken, P., Cao, Y., Zhou, Y., Kunz, J., and Bellen, H.J. (2005). The v-ATPase V0 subunit a1 is required for a late step in synaptic vesicle exocytosis in Drosophila. Cell *121*, 607–620.

56. Wu, M.N., Fergestad, T., Lloyd, T.E., He, Y., Broadie, K., and Bellen, H.J. (1999). Syntaxin 1A interacts with multiple exocytic proteins to regulate neurotransmitter release in vivo. Neuron *23*, 593–605.

57. Deitcher, D.L., Ueda, A., Stewart, B.A., Burgess, R.W., Kidokoro, Y., and Schwarz, T.L. (1998). Distinct requirements for evoked and spontaneous release of neurotransmitter are revealed by mutations in the Drosophila gene neuronal-synaptobrevin. J. Neurosci. *18*, 2028–2039.

58. DiAntonio, A., Parfitt, K.D., and Schwarz, T.L. (1993). Synaptic transmission persists in synaptotagmin mutants of Drosophila. Cell *73*, 1281–1290.

59. Bischof, J., Maeda, R.K., Hediger, M., Karch, F., and Basler, K. (2007). An optimized transgenesis system for Drosophila using germ-line-specific phiC31 integrases. Proc. Natl. Acad. Sci. USA *104*, 3312–3317.

60. Chotard, C., Leung, W., and Salecker, I. (2005). glial cells missing and gcm2 cell autonomously regulate both glial and neuronal development in the visual system of Drosophila. Neuron *48*, 237–251.

61. Mehta, S.Q., Hiesinger, P.R., Beronja, S., Zhai, R.G., Schulze, K.L., Verstreken, P., Cao, Y., Zhou, Y., Tepass, U., Crair, M.C., and Bellen, H.J. (2005). Mutations in Drosophila sec15 reveal a function in neuronal targeting for a subset of exocyst components. Neuron *46*, 219–232.

62. Rigort, A., Günther, D., Hegerl, R., Baum, D., Weber, B., Prohaska, S., Medalia, O., Baumeister, W., and Hege, H.C. (2012). Automated segmentation of electron tomograms for a quantitative description of actin filament networks. J. Struct. Biol. *177*, 135–144.

63. Weber, B., Greenan, G., Prohaska, S., Baum, D., Hege, H.C., Müller-Reichert, T., Hyman, A.A., and Verbavatz, J.M. (2012). Automated tracing of microtubules in electron tomograms of plastic embedded samples of Caenorhabditis elegans embryos. J. Struct. Biol. *178*, 129–138.

64. Scherer, M.K., Trendelkamp-Schroer, B., Paul, F., Pérez-Hernández, G., Hoffmann, M., Plattner, N., Wehmeyer, C., Prinz, J.H., and Noé, F. (2015). PyEMMA 2: a software package for estimation, validation, and analysis of Markov models. J. Chem. Theory Comput. *11*, 5525–5542.

65. Metzner, P., Schütte, C., and Vanden-Eijnden, E. (2009). Transition path theory for Markov jump processes. Multiscale Model. Simul. *7*, 1192–1219.

STAR★METHODS

KEY RESOURCES TABLE

REAGENT or RESOURCE	SOURCE	IDENTIFIER
Antibodies		
rabbit anti-Rab5	Abcam	ab31261, RRID: AB_882240
rabbit anti-Rab7	Gift from Patrick Dolph [53]	N/A
mouse anti-Rab11	BD Transduction Laboratories	Clone 47, RRID: AB_397983
rabbit anti-Syt1	Developmental Studies Hybridoma Bank (DSHB)	3H2 2D7, RRID: AB_528483
rabbit anti-GABARAP+GABARAPL1+GABARAPL2 (ATG8)	Abcam	ab109364, RRID: AB_10861928
guinea pig anti-Spin	Gift from Sean Sweeney [37]	N/A
rat anti-Sky	Gift from Patrik Verstreken [12]	N/A
mouse anti-CSP	DSHB	DCSP-2 (6D6), RRID: AB_528183
rabbit anti-Rab3	Gift from Aaron DiAntonio [54]	N/A
mouse anti-Syx1a	DSHB	8C3, RRID: AB_528484
guinea pig anti-V100	[55]	N/A
rabbit anti-n-Syb	[55]	N/A
rat anti-n-Syb (R29)	Gift from Hugo Bellen [56]	N/A
mouse anti-Chaoptin	DSHB	24B10, RRID: AB_528161
Cy5 AffiniPure Goat Anti-Rabbit IgG (H+L)	Jackson Immunoresearch	111-175-144, RRID: AB_2338013
Cy5 AffiniPure Goat Anti-Mouse IgG (H+L)	Jackson Immunoresearch	115-175-146, RRID: AB_2338713
Cy5 AffiniPure Goat Anti-Rat IgG (H+L)	Jackson Immunoresearch	112-175-143, RRID: AB_2338263
Alexa Fluor 647 AffiniPuree Goat Anti-Guinea Pig IgG (H+L)	Jackson Immunoresearch	106-605-003, RRID: AB_2337446
Cy3 AffiniPure Goat Anti-Rabbit IgG (H+L)	Jackson Immunoresearch	111-165-144, RRID: AB_2338006
Alexa Fluor 488 AffiniPure Goat Anti-Rabbit IgG (H+L)	Jackson Immunoresearch	111-545-144, RRID: AB_2338052
Chemicals, Peptides, and Recombinant Proteins		
TOTO3	Thermo Fisher	T3604
Vectashield	Vector Laboratories	H-1000
PBS	GIBCO	70011-36
Formaldehyde	Merck KGaA	1.03999.1000
Triton X-100	Sigma-Aldrich	T8787
Schneider's *Drosophila* Medium [+] L-Glutamine	GIBCO	21720-024
Agarose, low gelling temperature	Sigma-Aldrich	A9045-10G
Human insulin recombinant zinc	GIBCO	12585014
Penicillin/Streptomycin	GIBCO	15140122
ES Cell FBS	GIBCO	16141-061
20-Hydroxyecdysone	Sigma-Aldrich	5289-74-7
SilGard and Silicone Elastomer Kit	Dow Corning	184
Sodium Chloride	Merck KGaA	1.06404.1000
Experimental Models: Organisms/Strains		
Drosophila, UAS-myr-mCherry-pHluorin in VK00002	This paper	N/A
Drosophila, UAS-Syt1-mCherry-pHluorin in VK00002	This paper	N/A
Drosophila, UAS-mCherry-pHluorin-Syt1 in VK00002	This paper	N/A
Drosophila, UAS-CP1-mCherry-pHluorin in VK00002	This paper	N/A
Drosophila, GMR-Gal4	Bloomington Drosophila Stock Center (BDSC)	9146
Drosophila, ppk-Gal4	BDSC	32078
Drosophila, ey3.5flp	BDSC	35542

(*Continued on next page*)

Continued		
REAGENT or RESOURCE	SOURCE	IDENTIFIER
Drosophila, FRT82b,tub-Gal80	BDSC	5135
Drosophila, FRT80b,tub-Gal80	BDSC	5191
Drosophila, $nsyb^{F33B}$	[57]	N/A
Drosophila, $rab7^{gal4\text{-}knock\text{-}in}$	[17]	N/A
Drosophila, $v100^{4}$	[55]	N/A
Drosophila, syt^{AD4}	[58]	N/A
Drosophila, FRT40A,cl	BDSC	5622
Drosophila, UAS-Atg8-mCherry	BDSC	37749
Drosophila, UAS-Syt1-GFP	BDSC	6926
Drosophila, GMR-myr-GFP	BDSC	7112
Drosophila, GMR-myr-Tomato	Gift from S.Lawrence Zipursky	N/A
Drosophila, $car^{\Delta 146}$,FRT19A	Gift from Helmut Kramer	N/A
Drosophila, UAS-V100	[55]	N/A
Drosophila, UAS-n-Syb	[22]	N/A
Drosophila, UAS-Rab7	Hiesinger lab	N/A
Drosophila, UAS-n-Syb-RNAi	VDRC	104531
Recombinant DNA		
mCherry-SEpHluorin	Addgene	32001
pUASTattB	[59]	Flybase ID: FBmc0003002
Software and Algorithms		
ImageJ	National Institutes of Health (NIH)	N/A
Imaris	Bitplane, Switzerland	N/A
GraphPad Prism	GraphPad Software, La Jolla, USA	N/A
AutoQuant 3x	Media Cybernetics	N/A
Clampfit	Axon Instruments	N/A
Clampex	Axon Instruments	N/A
Python	Python Software Foundation	N/A
Amira	FEI-Thermo Fisher Scientific	N/A

CONTACT FOR REAGENT AND RESOURCE SHARING

Further information and requests for resources and reagents should be directed and will be fulfilled by the Lead Contact, Dr. Robin Hiesinger (robin.hiesinger@fu-berlin.de).

EXPERIMENTAL MODEL AND SUBJECT DETAILS

Fly husbandry

All flies were raised on standard molasses formulation food at either 25°C (most crosses), 29°C (RNAi crosses) or 21°C ($Gal80^{ts}$ crosses).

Flies

For live-imaging and fixed immunostainings, photoreceptor clones expressing the imaging probes were generated using the *ey3.5flp* system [60, 61] in otherwise heterozygous animals. For the analyses of myr-DF and Syt1-DF probes in control and mutant photoreceptors, the following *Drosophila* lines were used: control (ey3.5flp/+;GMR-Gal4/GMR-Gal4,UAS-myr-DF or UAS-Syt1-DF;FRT82B,tub-Gal80/FRT82B), *v100* (ey3.5flp/+;GMR-Gal4/GMR-Gal4,UAS-myr-DF or UAS-Syt1-DF;FRT82B,tub-Gal80/FRT82B,$v100^{4}$; Hiesinger et al., 2005), *n-syb* (ey3.5flp/+;GMR-Gal4/GMR-Gal4, UAS-myr-DF or UAS-Syt1-DF;FRT80B,tub-Gal80/FRT80B,$n\text{-}syb^{\Delta F33B}$; Deitcher et al., 1998), *rab7* (ey3.5flp/+;GMR-Gal4/GMR-Gal4,UAS-myr-DF or UAS-Syt1-DF;FRT82B,tub-Gal80/FRT82B,$rab7^{gal4\text{-}knock\text{-}in}$ [17]). For *syt1* rescue ERG recordings, the following *Drosophila* lines were used: control (eyflp/+;FRT40A,GMR-Gal4/FRT40A,cl^{w+}), *syt1* mutant (eyflp/+;FRT40A,syt^{AD4},GMR-Gal4/FRT40A, cl^{w+}), rescue by C-terminally tagged Syt1 (Syt1-DF) (eyflp/+;FRT40A,syt^{AD4},GMR-Gal4,UAS-Syt1-DF/FRT40A,cl^{w+}), rescue by N-terminally tagged Syt1 (DF-Syt1) (eyflp/+;FRT40A,syt^{AD4},GMR-Gal4,UAS-DF-Syt1/FRT40A,cl^{w+}). For class IV sensory neuron live-imaging: class IV neurons

(ppk-Gal4>UAS-Syt1-DF or UAS-myr-DF). For autophagy live-imaging experiments: (GMR-Gal4>UAS-Atg8-mCherry,UAS-Syt1-GFP), (GMR-Gal4>UAS-Atg8-mCherry,GMR-myr-GFP). For co-imaging of fluorescently tagged myr and Syt1 probes: (GMR-Gal4>UAS-Syt1-GFP,GMR-myr-Tomato). For n-Syb knockdown experiments: n-Syb knockdown in v100 mutant background (ey3.5flp/+;GMR-Gal4,UAS-myr-DF or UAS-Syt1-DF/UAS-nSyb-RNAi;FRT82b,*v100*/FRT82b,tub-Gal80), n-Syb knockdown (ey3.5flp/+;GMR-Gal4,UAS-myr-DF or UAS-Syt1-DF/UAS-nSyb-RNAi), control (ey3.5flp/+;GMR-Gal4,UAS-myr-DF or UAS-Syt1-DF/+). For overexpression experiments: (Gmr-Gal4,UAS-myr-DF or UAS-Syt1-DF/UAS-Rab7), (GMR-Gal4,UAS-myr-DF or UAS-Syt1-DF/UAS-V100), (Gmr-Gal4,UAS-myr-DF or UAS-Syt1-DF/UAS-n-Syb), control (GMR-Gal4,UAS-myr-DF or UAS-Syt1-DF/+). For *carnation* mutant experiment: carnation mutant (FRT19A,tub-Gal80,hsflp/FRT19A,car$^{\Delta 146}$;GMR-Gal4,UAS-myr-DF or UAS-Syt1-DF/+), control (FRT19A,tub-Gal80,hsflp/FRT19A;GMR-Gal4,UAS-myr-DF or UAS-Syt1-DF/+).

To generate *UAS-myr-mCherry-pHluorin*, we amplified DNA encoding the first 30 amino acids of *Drosophila Src64B* from P[UAS-myr-RFP] (donated from Henry Chang) and PCR amplified the *mCherry-pHluorin* sequence from the mCherry-SEpHluorin vector (addgene, plasmid #32001, donated by Sergio Grinstein), generated the final linear DNA 5′-*NotI-myr-linker-mCherry-pHluorin-XhoI*-3′ by overlap extension PCR, then cloned it into the pUASTattB vector. Linker sequence: GCT GCC. For the generation of UAS-*syt1-mCherry-pHluorin*, UAS-*mCherry-pHluorin-Syt1* and UAS-*CP1-mCherry-pHluorin* (CP1-DF), the same strategy was followed except *syt1* or *cp1* was amplified from a cDNA sample. All constructs were integrated in the same landing site (y^{1}w^{1118}; PBac[y[+]-attP-3B]VK00002) in *Drosophila* genome to equalize expression levels. Transgenic flies were generated using standard procedures through Rainbow Transgenicsm USA.

METHOD DETAILS

Brain culture and live imaging

Pupal eye-brain complexes were dissected in cold Schneider's *Drosophila* Medium and cultured in the culture chambers perfused with culture medium as previously described [29]. For adult photoreceptor live imaging, 1-day and 2-week old adult fly eyes were dissected, with the lamina attached to the retina. To fully expose lamina photoreceptor terminals, pupal brains were mounted dorsal side up and adult eyes were mounted lamina side up in 0.4% dialyzed low-melting agarose. For class IV neuron live imaging, L3 fillet preparation was performed in cold Schneider's *Drosophila* Medium in a SylGard-covered Petri dish.

Live imaging was performed at room temperature using a Leica TCS SP8 X confocal microscope with a resonant scanner, using 63X water objective (NA = 1.2), and optimized settings of minimal white laser excitation and cross-talk avoiding SP detector emission windows. White laser excitation was set to 488 nm for GFP and phluorin, 554 nm for tdTomato, and 587 nm for mCherry signal acquisitions.

Immunohistochemistry

Pupal and adult eye-brain complexes were dissected and collected in cold Schneider's *Drosophila* Medium. The tissues were fixed in PBS with 4% formaldehyde for 30 min and washed in PBST (PBS+0.4% Triton X-100). The following primary antibodies were used: rabbit anti-Rab5 (1:1000), rabbit anti-Rab7 (1:1000), mouse anti-Rab11 (1:1000), rabbit anti-Syt1 (1:1000), rabbit anti-GABARAP (1:100), guinea pig anti-Spin (1:1000), rat anti-Sky (1:200), mouse anti-CSP (1:50), rabbit anti-Rab3 (1:1000), mouse anti-Syx1a (1:50), guinea pig anti-V100 (1:1000), rabbit anti-n-Syb (1:1000), rat anti-nSyb (1:1000), mouse anti-Rst (1:500), mouse anti-Chaoptin (1:500). All samples were mounted in mounting medium (Vectashield; Vector Laboratories) for confocal microscopy. Secondary antibodies used were Cy3, Cy5 (Jackson ImmunoResearch Laboratories), and Alexa 488 (Invitrogen). High-resolution confocal microscopy was performed at room temperature using a Leica TCS SP8 X with 63X Glycerol objective (NA = 1.3). White laser excitation was set to 488 nm for Alexa488, 548 nm for Cy3, and 645 nm for Cy5 signal acquisitions.

Image processing

All 4D live-imaging data were deconvolved with either ImageJ (National Institute of Health) plug-in Microvolution (Microvolution, 2014-2016) or AutoQuant 3X (Media Cybernetics) using adaptive PSF (blind) prior to analysis. Data were processed using Imaris (Bitplane), ImageJ (National Institute of Health), Amira 6.3 (FEI - Thermo Fisher Scientific), Photoshop (CS6, Adobe, Inc) and Python-based software listed in the section 'Markov State Model'.

Electroretinogram (ERG) Recordings

1-day-old adult flies were reversibly glued on slides using nontoxic school glue. Flies were exposed to 1 s pulses of light stimulus provided by computer-controlled white light-emitting diode system (MC1500; Schott) as previously reported [20]. ERGs were recorded using Clampex (Axon Instruments) and measured using Clampfit (Axon Instruments).

QUANTIFICATION AND STATISTICAL ANALYSIS

Quantification and Statistical Analysis

For volume, number, fusion, fission, speed and partition analyses, all 4D live-imaging data were deconvolved with AUTO Quant 3x (Modality: Laser Scanning Confocal; Objective Lens: 1.2 NA; Num. Aperture: 1.2; Imm. Medium (RI): 1.33; Sample Medium (RI) Water (1.33), Dist. From Coverslip: 20; Deconvolution Method: Adaptive PSF (Blind); PSF Settings: Theoretical PSF; Deconvolution

Settings: Adaptive PSF, 10 Iterations, Medium Noise), and analyzed using IMARIS (Bitplane, Switzerland). Binarized datasets were generated semi-automatically, then 4D tracking was performed manually. The following measurements were obtained from the built-in statistics analyses tools of IMARIS: volume, number, speed. The following measurements were obtained manually: fusion and fission frequencies, maximum displacement. For colocalization experiments, the data were obtained in 3D and all co-localization quantification was performed manually on single slices. The following number of compartments were counted: (a) mCherry-only, (b) mCherry-pHluorin, (c) mCherry-only & antibody co-localization, (d) mCherry-pHluorin & antibody co-localization. Only discernible individual compartments were counted. Co-localization ratios were calculated as follows: Co-localization ratios of yellow compartments = d/(a+b), Co-localization ratio of red compartments = c/(a+b). In Figures 2F, 2H, 2J, and 2L, co-localization ratios were calculated as follows: Co-localization ratio of yellow compartments = d/b, Co-localization ratio of red compartments = c/a. All statistical analyses were performed in GraphPad Prism, and the statistical analyses and sample numbers used for each result are indicated in the figure legends.

Markov State Modeling

The image analysis was performed using Python 2.7.12 with scikit-image 0.14 and Amira 6.3. The image stacks were reduced to a single slice with a maximum intensity projection. Each frame was smoothed with a Gaussian kernel and the pHluorin channel was subtracted from the mCherry channel to reduce the background signal. The differential images from each time step were then stacked into a three-dimensional volume. To extract tubular structures in space-time, the normalized cross correlation with a solid cylinder template was performed on this volume [62, 63]. Areas with high correlation were traced to extract the compartment trajectories. To analyze the trajectories from the image analysis, a Markov state model (MSM) was defined with pyEMMA 2.4 [64], where each state represents an area of 8x8 pixels (600 states in a 60 by 10 grid). The state assignment for each compartment was computed with the negative exponential distance to each state, normalized to one. The products of the state vectors between two time points were summed and normalized to generate a stochastic transition matrix. This matrix was then used to compute the committor probabilities for each state [65]. The committor probability was here defined for a compartment to leave the image area retrograde rather than anterograde.

Current Biology, Volume *28*

Supplemental Information

Live Observation of Two Parallel Membrane Degradation Pathways at Axon Terminals

Eugene Jennifer Jin, Ferdi Ridvan Kiral, Mehmet Neset Ozel, Lara Sophie Burchardt, Marc Osterland, Daniel Epstein, Heike Wolfenberg, Steffen Prohaska, and Peter Robin Hiesinger

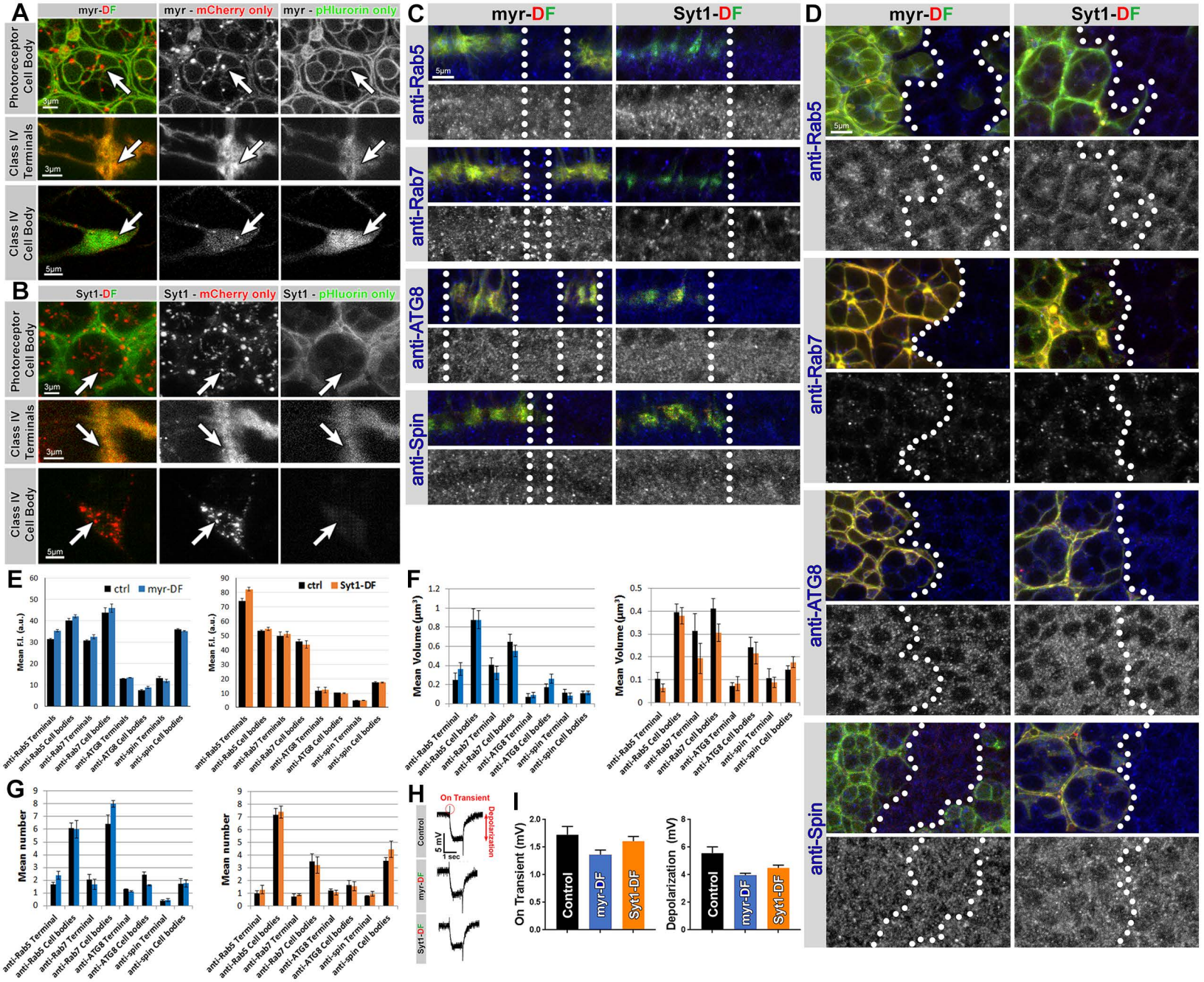

Figure S1. Myr-DF and Syt1-DF probes mark large acidic compartments in photoreceptor cell bodies, class IV da neuron axon terminals and cell bodies, and expression of neither probe affects endolysosomal and autophagic markers or photoreceptor function. Related to Figure 1.

(A and B) Live imaging of myr-DF (A) and Syt1-DF (B) reveal the presence of large acidic compartments in photoreceptor cell bodies at P+40%, class IV dendritic arborization neuron axon terminals and cell bodies. Arrows: examples of acidic (red-only live) compartments. (C and D) Comparison of the levels of endolysosomal and autophagic pathways markers (Rab5, early endosome; Rab7, late endosome/ multivesicular bodies (MVB); ATG8, autophagosome; Spin, lysosome) in mosaic expression of myr-DF or Syt1-DF at P+40% photoreceptor axon terminals (C) and cell bodies (D). The white dotted lines mark clonal boundaries (with and without probe expression). (E-G) Comparison of mean fluorescence (E), mean volume (F) and mean number (G) of endogenous endolysosomal markers in control (black) and probe-expressing [myr-DF (blue), Syt1-DF (orange)] axon terminals and cell bodies. Mean number per axon terminal was quantified, and mean number per ommatidium was quantified for cell bodies. Mean ± SEM, Unpaired t-test, brain n=3 per antibody staining. (H and I) Electroretinogram (ERG) recordings from adult photoreceptors expressing either myr-DF or Syt1-DF. Representative ERG traces (H), and quantifications of on-transient and depolarization amplitudes (I). Mean ± SEM, fly n=10 per genotype.

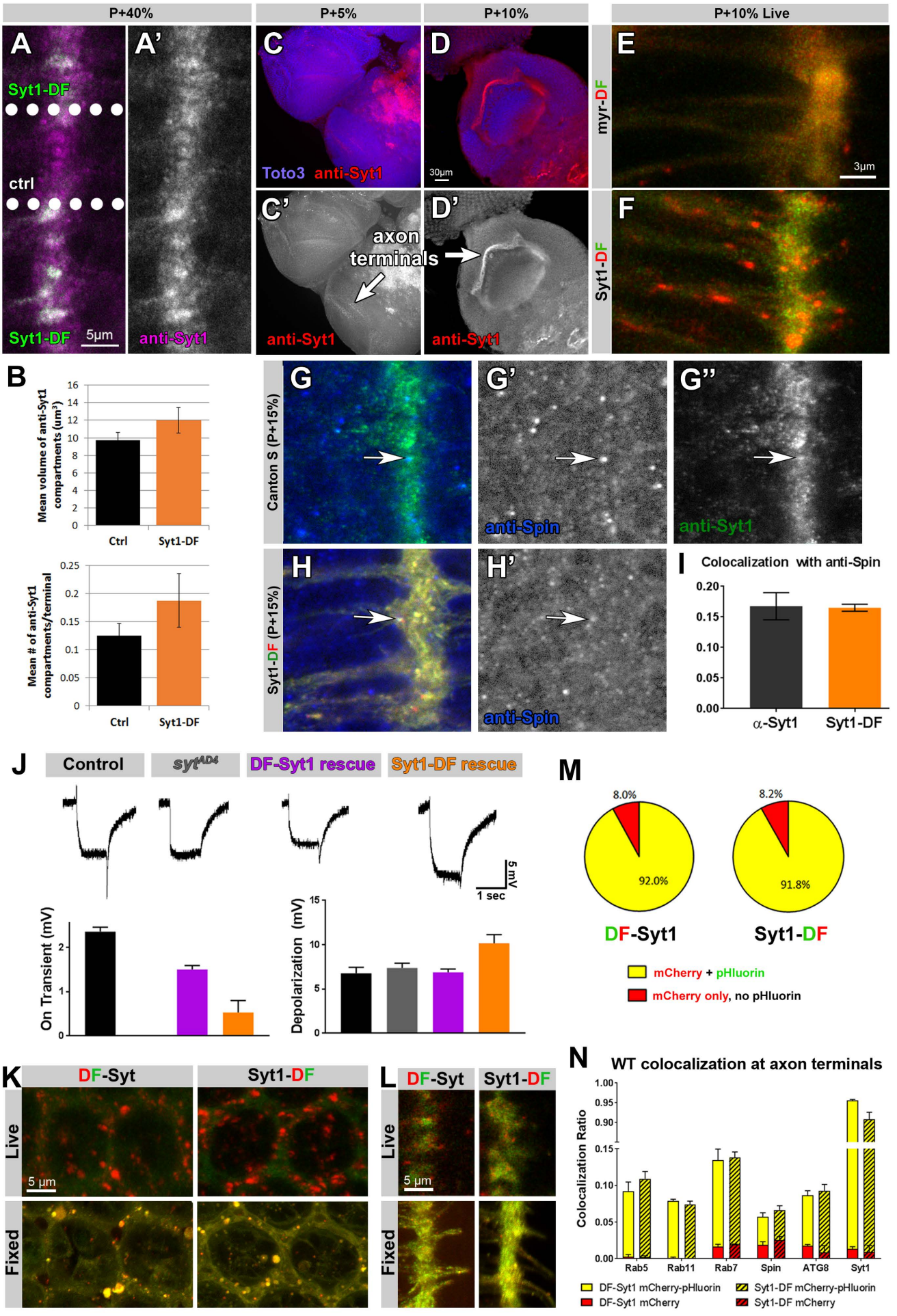
P+40%
P+5%
P+10%
P+10% Live
A
A'
Syt1-DF
ctrl
Syt1-DF
5µm
anti-Syt1
C
Toto3 anti-Syt1
D
30µm
E
myr-DF
3µm
C'
axon terminals
anti-Syt1
D'
anti-Syt1
F
Syt1-DF
B
Mean volume of anti-Syt1 compartments (um³)
Ctrl
Syt1-DF
Mean # of anti-Syt1 compartments/terminal
Ctrl
Syt1-DF
G
Canton S (P+15%)
G'
anti-Spin
G''
anti-Syt1
H
Syt1-DF (P+15%)
H'
anti-Spin
I
Colocalization with anti-Spin
α-Syt1
Syt1-DF
J
Control
syt4AD4
DF-Syt1 rescue
Syt1-DF rescue
5 mV
1 sec
On Transient (mV)
Depolarization (mV)
M
8.0%
92.0%
8.2%
91.8%
DF-Syt1
Syt1-DF
mCherry + pHluorin
mCherry only, no pHluorin
K
DF-Syt
Syt1-DF
Live
Fixed
5 µm
L
DF-Syt
Syt1-DF
Live
Fixed
5 µm
N
WT colocalization at axon terminals
Colocalization Ratio
Rab5
Rab11
Rab7
Spin
ATG8
Syt1
DF-Syt1 mCherry-pHluorin
DF-Syt1 mCherry
Syt1-DF mCherry-pHluorin
Syt1-DF mCherry

Figure S2. Syt1-DF is expressed at endogenous levels and sorted for degradation indistinguishably from endogenous Syt1, and cytoplasmically tagged Syt1-DF and lumenally tagged DF-Syt1 are indistinguishably localized and degraded in the endolysosomal pathway. Related to Figure 1.

(A-B) Antibody labeling with anti-Syt1 in mosaic expression of Syt1-DF in the P+40% photoreceptor axon terminals (A and A') and quantification of mean volume and number of compartments marked by anti-Syt1 (B). Mean ± SEM, brain n=3, Unpaired t-test. The white dotted lines mark clonal boundaries (with and without probe expression). (C-D') Endogenous Syt1 is localized to axon terminals of photoreceptors starting at 10% pupal development (P+10%). (E and F) Live imaging of myr-DF and Syt1-DF probes at P+10% photoreceptor axon terminals. Note that Syt1 protein turnover starts as soon as it is localized to photoreceptor terminals. (G-H') Syt1-DF colocalizes with lysosomal marker Spin equally as the endogenous Syt1 at P+15%. Arrows: colocalization of Syt1 compartments with anti-Spin. (I) Quantification of colocalization of endogenous Syt1 or Syt1-DF with anti-Spin at P+15%. Mean ± SEM, brain n=3 per experimental condition. (J) Rescue experiment of loss of neurotransmission of sytAD4 null mutant photoreceptors using either C- or N-terminally tagged Syt1 expression (Syt1-DF or DF-Syt1) in 1 day old adult flies. Representative ERG traces, and quantification of on-transient and depolarization amplitudes. Fly n=7 per genotype. (K and L) Live and fixed imaging of Syt1-DF and DF-Syt1 in cell bodies (K) and axon terminals (L) of P+40% photoreceptors. (M) Ratio of mCherry-only Syt1-DF and DF-Syt1 compartments at axon terminals after fixation. Brain n=15 per probe. (N) Colocalization of DF-Syt1 (non-striped) and Syt1-DF (striped) compartments with markers of endolysosomal system, autophagy and Syt1 antibody. Shown are ratios for 'yellow-fixed' and 'red-fixed' terminal hub compartments that colocalize with a given antibody divided by the total number of compartments. The 'yellow-fixed' and 'red-fixed' bars are stacked in the bar chart. Mean ± SEM, brain n=3 per antibody staining.

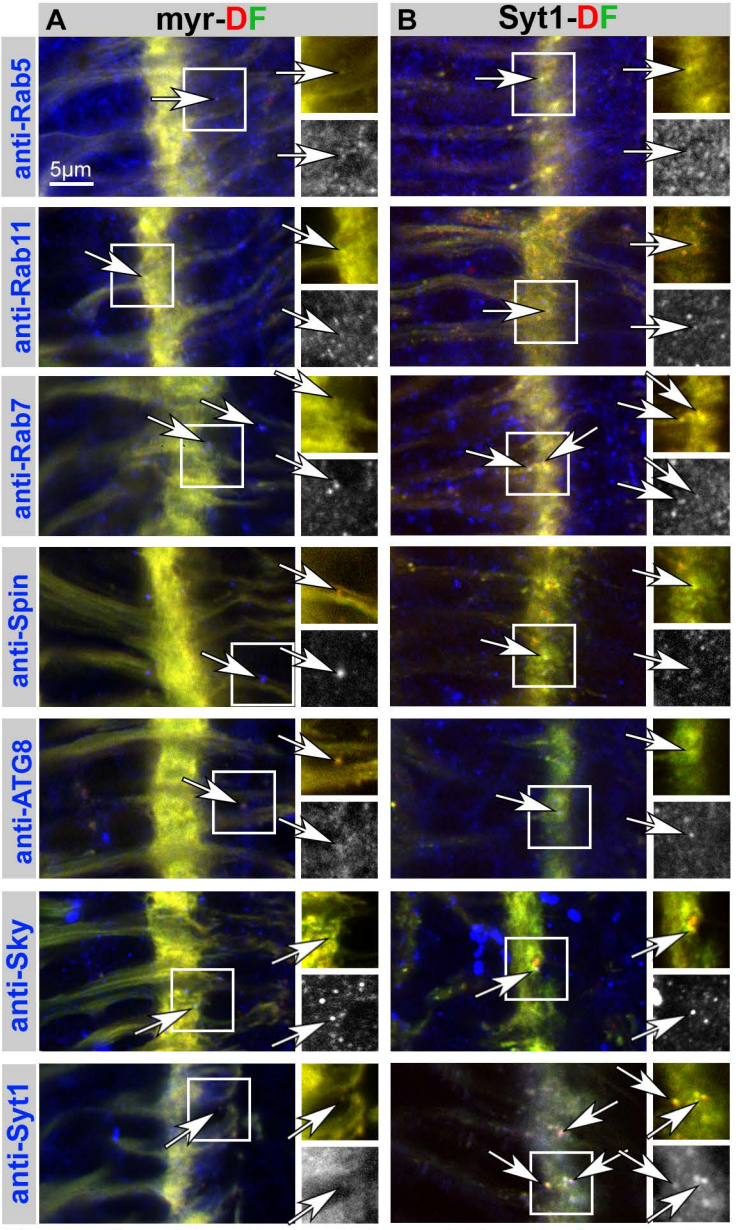

Figure S3. Colocalization of myr-DF or Syt1-DF probes with endolysosomal and autophagosomal markers at axon terminals. Related to Figure 2.

Representative images for colocalization of myr-DF (A) or Syt1-DF (B) at axon terminals with Rab5, Rab11, Rab7, Spinster (Spin), Atg8, Skywalker (Sky) and Synaptotagmin 1 (Syt1). Arrows: examples of colocalization. Single channels are antibody stainings.

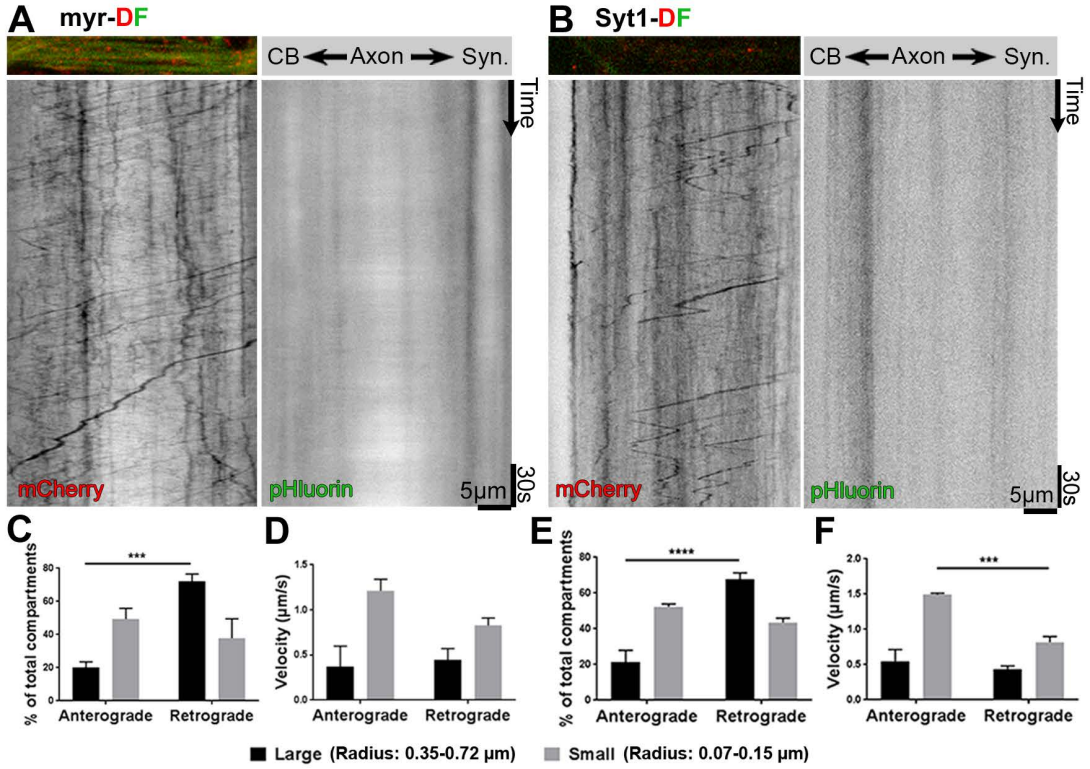
A
myr-DF
CB
Axon
Syn.
Time
mCherry
pHluorin
5μm
30s
B
Syt1-DF
CB
Axon
Syn.
Time
mCherry
pHluorin
5μm
30s

C
% of total compartments
***
Anterograde
Retrograde
D
Velocity (μm/s)
Anterograde
Retrograde
E
% of total compartments
****
Anterograde
Retrograde
F
Velocity (μm/s)
***
Anterograde
Retrograde
Large (Radius: 0.35-0.72 μm)
Small (Radius: 0.07-0.15 μm)

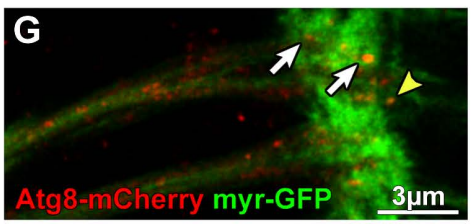
G
Atg8-mCherry myr-GFP
3μm

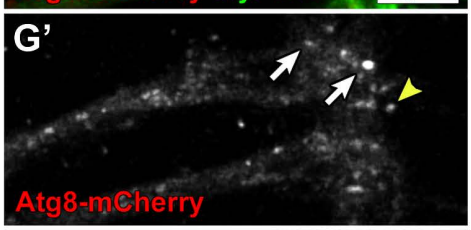
G'
Atg8-mCherry

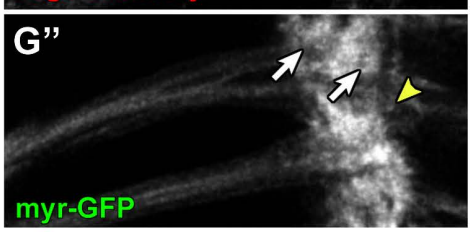
G''
myr-GFP

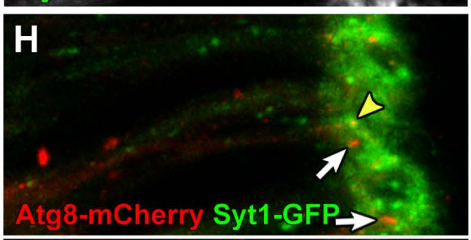
H
Atg8-mCherry Syt1-GFP

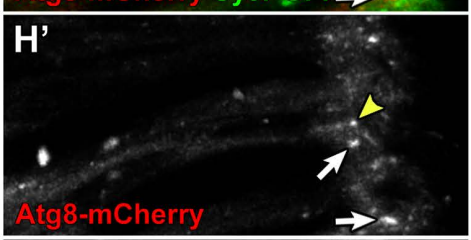
H'
Atg8-mCherry

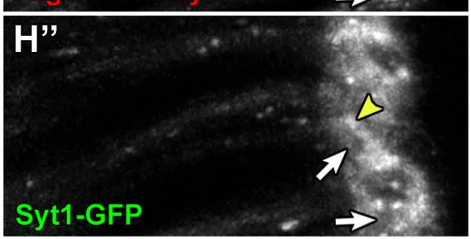
H''
Syt1-GFP

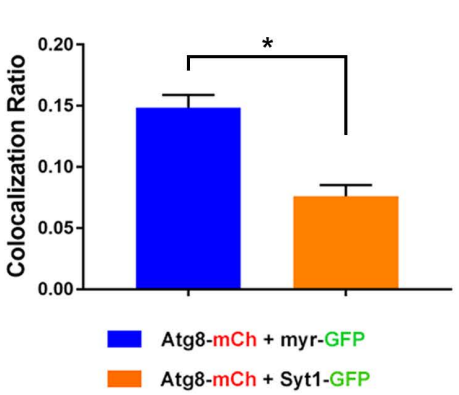
I
Colocalization Ratio
*
Atg8-mCh + myr-GFP
Atg8-mCh + Syt1-GFP

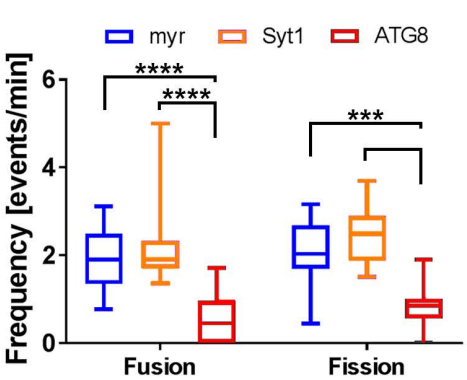
J
myr
Syt1
ATG8
Frequency [events/min]
****
****
***
Fusion
Fission

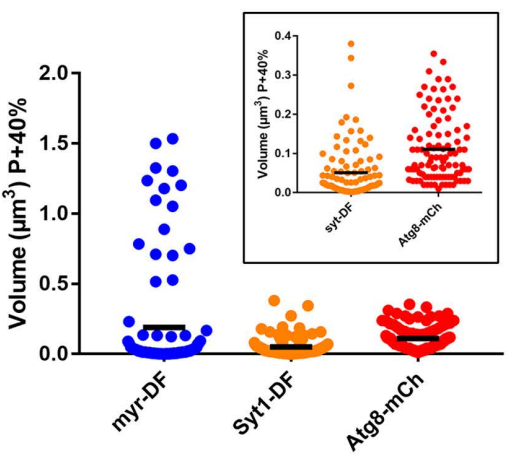
K
Volume (μm3) P+40%
myr-DF
Syt1-DF
Atg8-mCh
syt-DF
Atg8-mCh

Figure S4. Axonal transport dynamics of acidified axonal trafficking vesicles, and characteristics of autophagosomes compared to hub compartments. Related to Figure 3.

(A and B) Kymographs showing axonal transport of myr-DF (A) and Syt1-DF (B) positive compartments. (C and E) Net direction of large or small compartments positive for myr-DF (C) and Syt1-DF (E). Quantification for stationary compartments is not shown. Mean ± SEM, *** $p<0.001$, **** $p<0.0001$, Unpaired t-test, brain n=3 per probe. (D and F) Mean velocity of retrogradely or anterogradely trafficked compartments for myr-DF (D) and Syt1-DF (F). Mean ± SEM, *** $p<0.001$, **** $p<0.0001$, Unpaired t-test, brain n=3 per probe. (G-H'') Live imaging of co-expression of Atg8-mCherry and myr-GFP (G-G'') or Syt1-GFP (H-H'') at P+40% photoreceptor terminals and axons. White arrows: autophagosomes that do not co-localize with myr-GFP or Syt1-GFP positive compartments. Yellow arrowhead: autophagosomes that co-localize with myr-GFP or Syt1-GFP positive compartments. Stacks have been checked in 4D data for co-migration of autophagosomes and Syt1-GFP or myr-GFP positive compartments. (I) Quantification of colocalization ratio between Atg8-mCherry and myr-GFP or Syt1-GFP, Respectively. Mean ± SEM, * $p<0.05$, Unpaired t-test, brain n=3 per co-expression. (J) Fusion and fission frequencies of Atg8-mCherry positive autophagosomes compared to myr-DF and Syt1-DF positive acidified compartments. Box and whiskers plot, showing 5-95 percentiles, hub n=12 to 15 per probe, *** $p<0.001$, **** $p<0.0001$, Unpaired t-test. (K) Volumes of Atg8-mCherry compartments at axon terminals at P+40%, compared with acidified myr-DF and Syt1-DF from Figure 4D. Hub n=100 per probe, black lines indicate mean values. Inset compares volumes of Syt1-DF and Atg8-mCherry compartments.

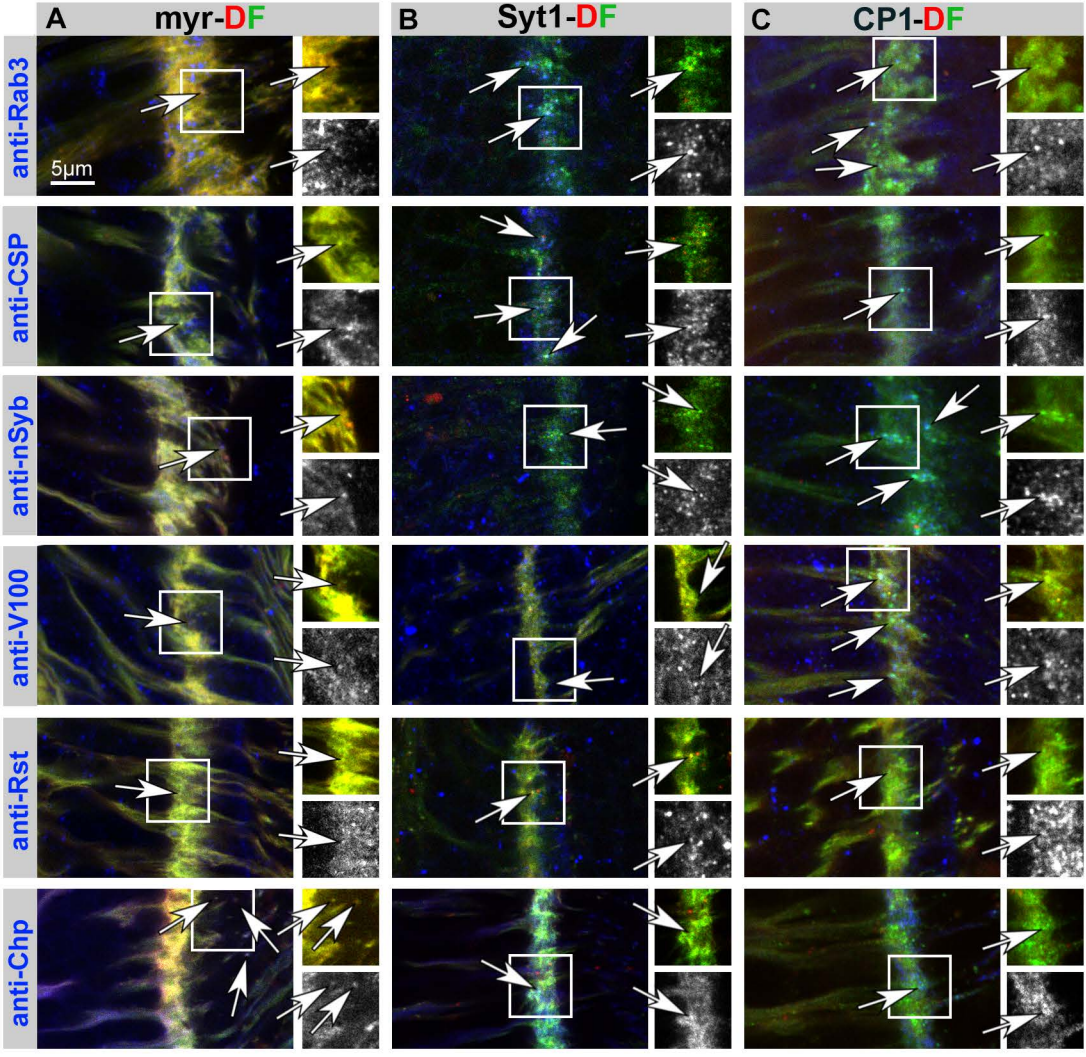

Figure S5. Colocalization of hub compartments at axon terminals with synaptic vesicle proteins and plasma membrane proteins. Related to Figure 4.

Representative images for colocalization of myr-DF (A), Syt1-DF (B), and CP1-DF (C) positive compartments with SV markers (Rab3, Cystein String Proteins (CSP)), SV and endolysosomal markers (neuronal Synaptobrevin (n-Syb) and vesicular ATPase component V100), and two photoreceptor plasma membrane receptors (Chaoptin (Chp) and Roughest (Rst)). Arrows: examples of colocalization. Single channels are antibody stainings.

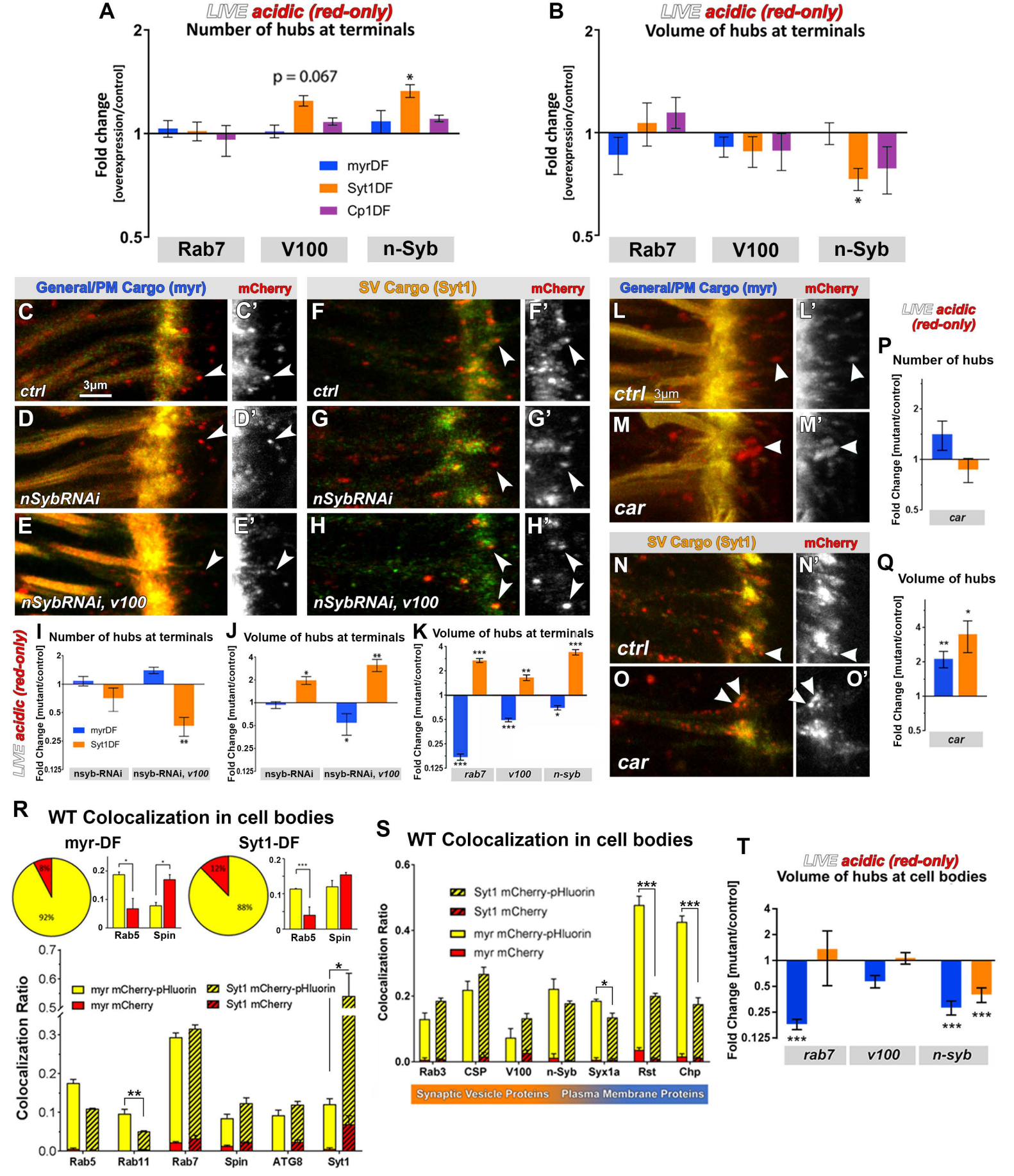
A
LIVE acidic (red-only)
Number of hubs at terminals
Fold change [overexpression/control]
p = 0.067
*
myrDF
Syt1DF
Cp1DF
Rab7
V100
n-Syb
B
LIVE acidic (red-only)
Volume of hubs at terminals
Fold change [overexpression/control]
*
Rab7
V100
n-Syb
General/PM Cargo (myr)
mCherry
SV Cargo (Syt1)
mCherry
C
C'
F
F'
ctrl
3µm
D
D'
G
G'
nSybRNAi
E
E'
H
H"
nSybRNAi, v100
General/PM Cargo (myr)
mCherry
L
L'
ctrl
3µm
M
M'
car
LIVE acidic (red-only)
P
Number of hubs
Fold Change [mutant/control]
car
SV Cargo (Syt1)
mCherry
N
N'
ctrl
O
O'
car
Q
Volume of hubs
Fold Change [mutant/control]
car
LIVE acidic (red-only)
I
Number of hubs at terminals
Fold Change [mutant/control]
myrDF
Syt1DF
nsyb-RNAi
nsyb-RNAi, v100
J
Volume of hubs at terminals
Fold Change [mutant/control]
nsyb-RNAi
nsyb-RNAi, v100
K
Volume of hubs at terminals
Fold Change [mutant/control]
rab7
v100
n-syb
R
WT Colocalization in cell bodies
myr-DF
Syt1-DF
8%
92%
12%
88%
Rab5
Spin
Colocalization Ratio
myr mCherry-pHluorin
myr mCherry
Syt1 mCherry-pHluorin
Syt1 mCherry
Rab5
Rab11
Rab7
Spin
ATG8
Syt1
S
WT Colocalization in cell bodies
Colocalization Ratio
Syt1 mCherry-pHluorin
Syt1 mCherry
myr mCherry-pHluorin
myr mCherry
Rab3
CSP
V100
n-Syb
Syx1a
Rst
Chp
Synaptic Vesicle Proteins
Plasma Membrane Proteins
T
LIVE acidic (red-only)
Volume of hubs at cell bodies
Fold Change [mutant/control]
rab7
v100
n-syb

Figure S6. Live and subcellular characterization of myr-DF and Syt1-DF marked compartments at axon terminals and cell bodies. Related to Figure 5.

(A and B) Relative number (A) and volume (B) of degradative compartments in Rab7, V100 or n-Syb overexpressing axon terminals. Mean ± SEM, * $p<0.05$, Unpaired t-test, brain n=3 per experimental condition. (C-H') Live imaging of myr-DF and Syt1-DF in n-Syb knockdown (n-Syb RNAi) or n-Syb knockdown in v100 mutant background at P+40% photoreceptor axon terminals. Arrowheads: examples of acidic (red-only live) compartments at axon terminals. (I and J) Relative number (I) and volume (J) of degradative compartments from live imaging data shown in A-F'. Mean ± SEM, * $p<0.05$, ** $p<0.01$, Unpaired t-test, brain n=3 per experimental condition. (K) Relative volume of acidic compartments in mutants from live imaging data at axon terminals (Figure 5A-5H'). Mean ± SEM, * $p<0.05$, ** $p<0.01$, *** $p<0.001$, Kolmogorov-Smirnov test, hub n=240 to 1314, brain n=3 per experimental condition. (L-O') Live imaging of myr-DF and Syt1-DF in car mutant background at P+40% photoreceptor axon terminals. Arrowheads: examples of acidic (red-only live) compartments at axon terminals. (P and Q) Relative number (P) and volume (Q) of acidic compartments in car mutant live imaging data. Mean ± SEM, * $p<0.05$, ** $p<0.01$, Unpaired t-test, brain n=3 per experimental condition. (R) Wildtype colocalization of myr-DF and Syt1-DF compartments in cell bodies. Pie charts show ratios of 'red-fixed' vs 'yellow-fixed' compartments in cell bodies. Bar charts show colocalization ratios of 'yellow-fixed' and 'red-fixed' compartments separately with early endosomal marker Rab5 and lysosomal marker Spin. Bar chart on the bottom shows wildtype colocalization of myr-DF (non-striped) and Syt1-DF (striped) compartments with markers of endolysosomal system, autophagy and Syt1 antibody in cell bodies. Shown are ratios for 'yellow-fixed' and 'red-fixed' compartments that colocalize with a given antibody divided by the total number of compartments. The 'yellow-fixed' and 'red-fixed' bars are stacked in the bar chart. Mean ± SEM, Unpaired t-test, * $p<0.05$, ** $p<0.01$, *** $p<0.01$, brain n=3 to 5. (S) Wildtype colocalization of myr-DF (non-striped) and Syt1-DF (striped) compartments with markers of SV proteins and plasma membrane proteins in cell bodies. Shown are ratios for 'yellow-fixed' and 'red-fixed' compartments that colocalize with a given antibody divided by the total number of compartments. The 'yellow-fixed' and 'red-fixed' bars are stacked in the bar chart. Mean ± SEM, Unpaired t-test, * $p<0.05$, *** $p<0.001$, brain n=3 per antibody staining. (T) Relative volume of acidic compartments in mutants from live imaging data in cell bodies. Mean ± SEM, *** $p<0.001$, Kolmogorov-Smirnov test, hub n=240 to 1314, brain n=3 per experimental condition.

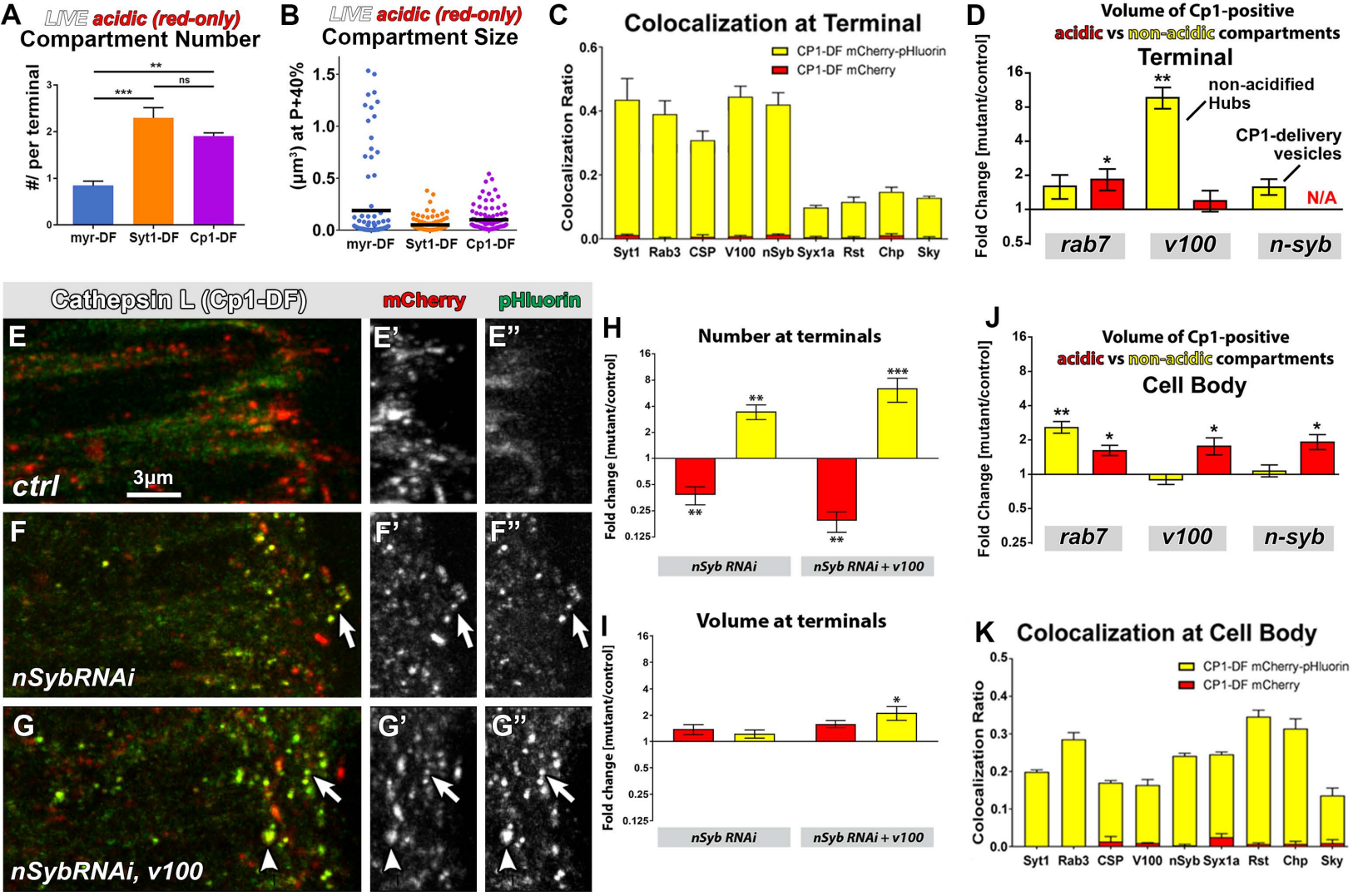

Figure S7. Live and subcellular characterization of CP1-DF marked compartments at axon terminals and cell bodies. Related to Figure 6.

(A and B) Mean number (A) and volume (B) of acidified CP1-DF compartments per axon terminal at P+40% compared to myr-DF and Syt1-DF. n=100 per probe for volume analysis, black lines indicate mean values (B), mean ± SEM (A), **p < 0.01, ***p < 0.001, Unpaired t-test, brain n=3 per probe. (C) Wild-type colocalization of CP1-DF compartments with markers of SV proteins and plasma membrane proteins at axon terminals. Shown are ratios for 'yellow-fixed' and 'red-fixed' terminal compartments that colocalize with a given antibody divided by the total number of compartments. The 'yellow-fixed' and 'red-fixed' bars are stacked in the bar chart. Brain n=3 per antibody staining. (D) Relative volumes of non-acidic (yellow) and acidic (red) compartments containing CP1-DF in rab7, v100 or nsyb mutant backgrounds at axon terminals. Mean ± SEM, * p<0.05, ** p<0.01, Unpaired t-test, brain n=3 per experimental condition. (E-G") Live imaging of CP1-DF in n-Syb knockdown (n-Syb RNAi) or n-Syb knockdown in v100 mutant background at P+40% photoreceptor axon terminals. Arrows: small CP1-delivery vesicles. Arrowheads: large non-acidified hubs. (H and I) Relative number (H) and volume (I) of non-acidic (yellow) and acidic (red) compartments containing CP1-DF in n-Syb knockdown (n-Syb RNAi) or n-Syb knockdown in v100 mutant background at axon terminals. Mean ± SEM, * p<0.05, ** p<0.01, *** p<0.001, Unpaired t-test, brain n=3 per experimental condition. (J) Relative volumes of non-acidic (yellow) and acidic (red) compartments containing CP1-DF in rab7, v100 or nsyb mutant backgrounds in cell bodies. Mean ± SEM, * p<0.05, ** p<0.01, Unpaired t-test, brain n=3 per experimental condition. (K) Wild-type colocalization of CP1-DF compartments with markers of SV proteins and plasma membrane proteins in cell bodies. Shown are ratios for 'yellow-fixed' and 'red-fixed' compartments that colocalize with a given antibody divided by the total number of compartments. The 'yellow-fixed' and 'red-fixed' bars are stacked in the bar chart. Brain n=3 per antibody staining.

Probe, Genotype	Fusion			Fission			Speed			Max. displacement (up to 15 min tracks)		
	Mean [/min]	SEM	Range	Mean [/min]	SEM	Range	Mean [/min]	SEM	Range	Mean [/min]	SEM	Range
myr-DF, Control	1.93	0.21	0.77 - 3.11	2.02	0.24	0.44 - 3.16	5.99	0.51	3.39 - 10.3	2.33	0.22	1.3 - 3.7
myr-DF, *rab7 mutant*		--			--		5.88	0.67	2.73 - 12.4	1.99	0.26	0.9 - 3.6
myr-DF, *v100 mutant*	1.93	0.23	1.04 - 3.36	2.58	0.21	1.19 - 3.82	5.20	0.47	2.37 - 8.60	2.43	0.34	0.7 - 5.2
myr-DF, *nsyb mutant*	1.92	0.24	0.92 - 3.39	2.59	0.27	1.42 - 4.88	5.75	0.42	5.03 - 9.54	2.67	0.47	0.9 - 5.9
Syt1-DF, Control	2.21	0.27	1.35 - 5.00	2.47	0.20	1.50 - 3.69	6.00	0.32	4.48 - 8.47	2.74	0.26	1.2 - 4.1
Syt1-DF, *rab7 mutant*	1.36	0.17	0 - 1.98	1.66	0.15	0.55 - 2.44	5.57	0.49	3.16 - 10.50	2.33	0.15	1.4 - 3.1
Syt1-DF, *v100 mutant*	1.62	0.27	0.44 - 3.57	2.04	0.30	0 - 3.57	5.03	0.42	2.70 - 7.77	1.96	0.33	0.7 - 4.1
Syt1-DF, *nsyb mutant*	1.83	0.17	0.55 - 2.65	2.28	0.29	0.73 - 3.97	6.33	0.46	4.14 - 9.34	2.99	0.50	0.5 - 6.2
ATG8-mCherry-GFP	0.51	0.13	0 - 1.71	0.79	0.11	0 - 1.90	5.53	0.45	3.01 - 8.05	1.99	0.36	0.1 - 5.2

Table S1. Quantitative features of hub compartment dynamics. Related to Figure 3.